

**OPTICAL CHARACTERIZATION OF NANOSCALE
DIELECTRIC FILMS ON CURVED SURFACES
USING NEAR FIELD DIFFRACTION METHOD**

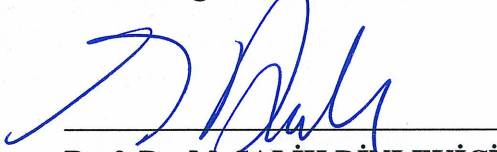
**A Thesis Submitted to
the Graduate School of Engineering and Sciences of
İzmir Institute of Technology
in Partial Fulfillment of the Requirements for the Degree of
MASTER OF SCIENCE
in Electronics and Communication Engineering**

**by
Enes ATAÇ**

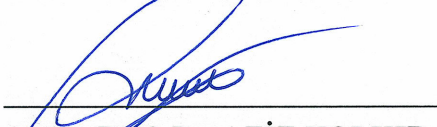
**June 2019
İZMİR**

We approve the thesis of **Enes ATAÇ**

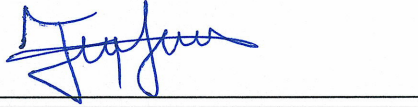
Examining Committee Members:



Prof. Dr. M. SALİH DİNLEYİCİ
Department of Electrical and Electronics Engineering
İzmir Institute of Technology



Assist. Prof. Dr. AZİZ KOLKIRAN
Department Of Nanoscience and Nanotechnology
İzmir Katip Çelebi University

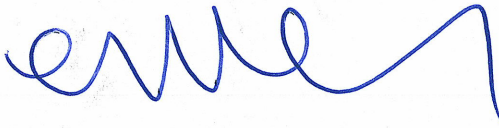


Assist. Prof. Dr. FATİH YAMAN
Department of Electrical and Electronics Engineering
İzmir Institute of Technology

26 June 2019



Prof. Dr. M. Salih DİNLEYİCİ
Supervisor, Department of Electrical and Electronics Engineering
İzmir Institute of Technology



Prof. Dr. Enver TATLICIOĞLU
Head of the Department of
Electrical and Electronics Engineering

Prof. Dr. Aysun SOFUOĞLU
Dean of the Graduate School of
Engineering and Sciences

ACKNOWLEDGMENTS

First of all, I owe a great deal of thanks to my supervisor Prof. Dr. M. Salih Dinleyici for his excellent guidance, tolerance and patience in every stage of my thesis study.

I would like to thank committee members for giving me support and contribution about every pages of the thesis.

I would like to express my sincere thanks to Çağın Ekici, Simay Yılmaz and Önder Yılmaz for their supports, helps and favours.

Special thanks to the colleagues Onur Cirit, Esra Tunçer, Orkan Olcay and İrem Öcal for their helpful suggestions and friendship.

Finally, I thank my mother Fahriye Ataç, my father Hüseyin Ataç and my sister Özge Ataç a lot for their true and invaluable support.

ABSTRACT

OPTICAL CHARACTERIZATION OF NANOSCALE DIELECTRIC FILMS ON CURVED SURFACES USING NEAR FIELD DIFFRACTION METHOD

Demand on the high-quality optical thin films has increased because of the importance in the optical sensor technologies. The thicknesses of such films are usually shorter than the wavelength of visible light. Therefore, the optical characterization of these films is not a routine procedure especially on curved surfaces such as optical fiber. Besides, the methods in the literature and commercially available systems are either expensive, destructive or non-real time. In this thesis, it is aimed to propose a simple, inexpensive and non-destructive optical characterization method of nano-scale dielectric films on curved surfaces. The methodology of that approach can be described as the near field wave-front tracing diffraction by using structured light. In this way, it has been shown that sub-wavelength film thicknesses can be estimated.

The proposed diffraction method is organized in four main stages. These are the coating of optical fibers, generation of structured light, determination of wave propagation via the near field Huygens-Fresnel wave-front tracing and sensing and processing of signal from the sensor array. Layer by layer assembly technique is used in coating process to keep under control the thickness of transparent film. Selection of various source types is about to changing of point spread function of applied field and observe the effects on intensity pattern. Using near field diffraction technique, sub-wavelength thickness of thin films can be predicted by taking the higher order components of diffraction pattern by recording at very close proximity to object. In this way, determination of thickness beyond the diffraction limits can be realized. Furthermore, the resolution of sensor array in sensing part is important since pixel size of the sensor array determines your detection limits to catch all variations on diffraction pattern. The whole process has a mathematical model with numerical analysis methods.

This dissertation is about the proposing a mathematical estimation model for the optical properties of nano-scale dielectric films coated on curved surfaces. The experimental results show that near field Huygens-Fresnel wave-front tracing method by using structured light is a powerful technique.

ÖZET

YAKIN ALAN DİFRAKSİYON YÖNTEMİ KULLANILARAK EĞİMLİ YÜZEYLERDEKİ NANO BOYUTLU YALITKAN FİMLERİN OPTİK KARAKTERİZASYONU

Yüksek kalitedeki ince optik filmlere olan talep optik sensör teknolojilerindeki önemi sebebiyle artmaktadır. Bu tür filmlerin kalınlıkları genellikle görünür ışığın dalga boyundan daha kısadır. Bu nedenle, bu filmlerin optik karakterizasyonu özellikle fiber optik gibi eğri yüzeylerde sıradan bir prosedür değildir. Ayrıca, literatürdeki yöntemler ve ticari olarak temin edilebilir sistemler pahalı, tahrip edici veya gerçek zamanlı değildir. Bu tez çalışmasında eğri yüzeylerde nano ölçekli dielektrik filmlerin basit, ucuz ve tahribatsız optik karakterizasyonu yönteminin önerilmesi amaçlanmıştır. Önerilen yöntem metodolojisi, yapılandırılmış ışık kullanılarak yakın alan Huygens Fresnel kırınımı dalga yüzü izleme olarak tanımlanabilir. Bu şekilde, dalga boyu altı film kalınlıklarının tahminlenebilir olduğu gösterilmeye çalışılmıştır.

Önerilen kırınım yöntemi dört ana aşamadan oluşmaktadır. Bunlar fiber optiğin kaplanması, yapılan-dırılmış ışığın oluşturulması, yakın alan Huygens-Fresnel dalga yüzü izlenerek dalga yayılımının belirlenmesi, duyuca diziliminden gelen sinyallerin algılanması ve işlenmesi. Saydam filmin kalınlığını ayarlayabilmek için kaplama işleminde katman katman birleştirme tekniği kullanılmıştır. Farklı kaynak tiplerinin seçimi dalganın nokta yayılma fonksiyonunun değiştirilmesi ve bu değişimin yoğunluk deseninde gözlemlenmesiyle alakalıdır. Yakın alan kırınım tekniğini kullanarak, ince filmlerin alt dalga boyu kalınlığı, nesneye çok yakın bir noktada kayıt yaparak dalganın yüksek uzaysal frekans bileşenlerini alarak tahmin edilebilir. Bu şekilde, kırınım sınırlarının ötesindeki kalınlığın belirlenmesi gerçekleştirilebilir. Ayrıca, algılayıcı diziliminin piksel boyutu tespit sınırlarını belirlediğinden, algılama bölümünde algılayıcı diziliminin seçimi önemlidir. Tüm süreç nümerik analiz yöntemlerini içeren matematiksel bir modele sahiptir.

Bu tez, eğri yüzeylerde kaplanmış nano ölçekli dielektrik filmlerin optik özellikleri için bir matematiksel tahmin modeli önermekle ilgilidir. Deneysel sonuçlar, yapılandırılmış ışık kullanılarak yakın alan Huygens-Fresnel dalga-ön izleme yönteminin, güçlü bir teknik olduğunu göstermektedir.

TABLE OF CONTENTS

| | |
|---|------|
| LIST OF FIGURES | viii |
| LIST OF ABBREVIATIONS | xi |
| CHAPTER 1. INTRODUCTION | 1 |
| 1.1. Optical Characterization Techniques | 1 |
| 1.2. Review of the Thesis | 2 |
| CHAPTER 2. THEORY AND MATHEMATICAL PRELIMINARIES | 4 |
| 2.1. Diffraction | 4 |
| 2.1.1. Kirchoff Diffraction Theory | 4 |
| 2.2. Diffraction Limit | 10 |
| 2.3. Structured Lightwave Generation | 14 |
| 2.3.1. Modal Structured Lightwaves | 18 |
| CHAPTER 3. MATHEMATICAL MODEL | 22 |
| 3.1. Diffraction from Cylindrical Objects | 22 |
| 3.1.1. Plane Wave | 23 |
| 3.1.1.1. Paraxial Ray Tracing | 23 |
| 3.1.1.2. Exact Ray Tracing | 26 |
| 3.1.2. Structured Light Modes | 28 |
| CHAPTER 4. EXPERIMENTAL SETUP, MEASUREMENTS AND RESULTS ... | 32 |
| 4.1. Experimental Setup | 32 |
| 4.2. Measurement Results | 35 |
| 4.2.1. Plane Wave Results | 37 |
| 4.2.2. LP01 Mode Results | 41 |
| 4.2.3. LP11 Mode Results | 45 |
| 4.2.4. Comparisons of Results | 51 |
| 4.3. Discussion | 53 |
| CHAPTER 5. CONCLUSION AND FUTURE WORKS | 55 |

REFERENCES 57

LIST OF FIGURES

| <u>Figure</u> | <u>Page</u> |
|--|-------------|
| Figure 2.1. Fresnel Zones | 5 |
| Figure 2.2. Surface of integration | 6 |
| Figure 2.3. Illustration of integration surface(a) and boundary conditions | 7 |
| Figure 2.4. Illustration of new boundaries | 8 |
| Figure 2.5. A system used for the calculation of PSF (Novotny and Hecht, 2012) ... | 10 |
| Figure 2.6. Illustration of diffraction limits of two point sources separated from each other Δr | 13 |
| Figure 2.7. Cylindrical geometry cross section (Balanis, 2012) | 15 |
| Figure 2.8. Bessel first kind and second kind functions | 17 |
| Figure 2.9. Modified Bessel first kind and second kind functions | 17 |
| Figure 3.1. (a) Plane wave passing through cylindrical object, (b) Diffraction from cylindrical object | 24 |
| Figure 3.2. Optical path lengths for different regions | 25 |
| Figure 3.3. The optical path for a ray | 26 |
| Figure 3.4. Simulations of the normalized intensity distributions 100 nm coated optical fiber diffraction pattern in air where the distance is 5cm with the observation plane, exact tracing(red) and paraxial tracing(blue) | 28 |
| Figure 3.5. Optical fiber geometry for far field calculations (Gambling et al., 1976) | 29 |
| Figure 3.6. (a) Linearly polarized field passing through cylindrical object, (b) Diffraction from cylindrical object | 30 |
| Figure 4.1. Schematic of the layer-by-layer deposition process (Yang et al., 2011) .. | 33 |
| Figure 4.2. Experimental setup for estimation of thickness by using plane wave | 33 |
| Figure 4.3. Intensity distributions of LP_{01} and LP_{11} at the beginning of coated fiber | 34 |
| Figure 4.4. Experimental setup for estimation of thickness by using structured light | 34 |
| Figure 4.5. Applied source intensity patterns: (a) LP01 mode (b) LP11 mode | 35 |
| Figure 4.6. Focal points of core and cladding | 36 |
| Figure 4.7. Deviation between non-coated and 70 nm coated fiber for different distances between optical fiber and sensor array (LP11 illumination) | 36 |
| Figure 4.8. Non-coated optical fiber-1: The experimental intensity fitted at non- coating of optical fiber | 37 |

| | |
|---|----|
| Figure 4.9. (a) Diffraction pattern recorded by sensor array (b) SEM result of non-coated optical fiber | 37 |
| Figure 4.10. Polymer coated optical fiber-2: The experimental intensity fitted at 180 nm coated optical fiber | 38 |
| Figure 4.11. (a) Diffraction pattern recorded by sensor array (b) SEM result of coated optical fiber about 183.5 nm | 38 |
| Figure 4.12. Polymer coated optical fiber-3: The experimental intensity fitted at 79 nm coated optical fiber | 39 |
| Figure 4.13. (a) Diffraction pattern recorded by sensor array (b) SEM result of coated optical fiber about 67 nm | 39 |
| Figure 4.14. Plane wave experimental results of non-coated and 180 nm coated optical fibers | 40 |
| Figure 4.15. Plane wave experimental results of non-coated and 79 nm coated optical fibers | 40 |
| Figure 4.16. Non-coated optical fiber-1: The experimental intensity fitted at non-coating of optical fiber | 41 |
| Figure 4.17. (a) Diffraction pattern recorded by sensor array (b) SEM result of non-coated optical fiber | 41 |
| Figure 4.18. Polymer coated optical fiber-2: The experimental intensity fitted at 179 nm coated optical fiber | 42 |
| Figure 4.19. (a) Diffraction pattern recorded by sensor array (b) SEM result of coated optical fiber about 183.5 nm | 42 |
| Figure 4.20. Polymer coated optical fiber-3: The experimental intensity fitted at 77 nm coated optical fiber | 43 |
| Figure 4.21. (a) Diffraction pattern recorded by sensor array (b) SEM result of coated optical fiber about 67 nm | 43 |
| Figure 4.22. LP01 mode experimental results of non-coated and 179 nm coated optical fibers | 44 |
| Figure 4.23. LP01 mode experimental results of non-coated and 77 nm coated optical fibers | 44 |
| Figure 4.24. Non-coated optical fiber-1: The experimental intensity fitted at non-coating of optical fiber | 45 |
| Figure 4.25. (a) Diffraction pattern recorded by sensor array (b) SEM result of non-coated optical fiber | 45 |
| Figure 4.26. Error-Thickness variation for non-coated optical fiber | 46 |

| | |
|---|----|
| Figure 4.27. Polymer coated optical fiber-2: The experimental intensity fitted at 187 nm coated optical fiber | 46 |
| Figure 4.28. (a) Diffraction pattern recorded by sensor array (b) SEM result of coated optical fiber about 183.5 nm | 47 |
| Figure 4.29. Error-Thickness variation for 187 nm coated optical fiber | 47 |
| Figure 4.30. Polymer coated optical fiber-3: The experimental intensity fitted at 70 nm coated optical fiber | 48 |
| Figure 4.31. (a) Diffraction pattern recorded by sensor array (b) SEM result of coated optical fiber about 67 nm | 48 |
| Figure 4.32. Error-Thickness variation for 70 nm coated optical fiber | 49 |
| Figure 4.33. LP11 mode theoretical results of non-coated and 187 nm coated optical fibers | 49 |
| Figure 4.34. LP11 mode experimental results of non-coated and 187 nm coated optical fibers | 50 |
| Figure 4.35. LP11 mode theoretical results of non-coated and 70 nm coated optical fibers | 50 |
| Figure 4.36. LP11 mode experimental results of non-coated and 70 nm coated optical fibers | 51 |
| Figure 4.37. Simulation results of diffraction patterns for various sources | 51 |
| Figure 4.38. Experimental results of diffraction patterns for various sources | 52 |
| Figure 4.39. Non-coated optical fiber simulation and experimental results for plane wave, LP01 and LP11 | 52 |
| Figure 4.40. 67 nm coated optical fiber simulation and experimental results for plane wave, LP01 and LP11 | 53 |
| Figure 4.41. 183.5 nm coated optical fiber simulation and experimental results for plane wave, LP01 and LP11 | 53 |
| Figure 5.1. LP11 mode simulation results of non-coated and 45 nm coated optical fibers | 56 |

LIST OF ABBREVIATIONS

| | |
|-----|------------------------------|
| LBL | Layer by Layer Assembly |
| LP | Linearly Polarized |
| M | Magnification Factor |
| NA | Numerical Aperture |
| PAA | Polyacrylic acid |
| PEI | Polyethylenimine |
| PSF | Point Spread Function |
| SEM | Scanning Electron Microscope |
| SPR | Surface Plasmon Resonance |

CHAPTER 1

INTRODUCTION

Optical phenomena can be mainly described as the interaction between electromagnetic radiation and matter. If this interaction takes place at the sub-wavelength scale, it becomes an interest area of nano-optics. Since Maxwell equations are adequate to describe optical radiation in nano-optics, wave approach is mostly used to describe optical radiation in nano-scales.

Optical resolution can be defined as a measure of the ability of how closely point-like objects can be distinguished. It is limited by the wavelength of the light which is called diffraction limit. Diffraction limit definition can be versatile depending on using of dipole sources instead of point sources or orientation of dipoles. According to the diffraction limits, it was not seem possible to express the interaction on nano-scales that are less than roughly half of the wavelength. Nevertheless, some techniques (Vangindertael et al., 2018) such as photon tunneling microscopy, near field scanning optical microscopy, confocal microscopy etc. have overcome the diffraction limit in last decades. This advancements offer an insight into super-resolution microscopy.

Optical characterization has an important role sensor in technologies, such as SPR sensors, since the components of system has to be monitored and verified. However, it must reach to resolution less than the dimensions of the structures since the properties and behaviour of structures such as thin films should be obtained accurately. Therefore, there are needed methods beyond diffraction limits.

1.1. Optical Characterization Techniques

Optical characterization can be defined as the determination of material characteristics, geometry and roughness using the variation of properties of light such as intensity, coherence phase, polarization, direction etc. These properties change after light-material interaction and carry valuable information since optical properties strongly affected by material structural, electronic and physical properties (Sardela, 2014). Besides, when optical characterization is compared with other techniques, it takes an advantages because of being non-invasive, non contact, real time and simple.

The first glance into the characterization was realized by the discovery of optical microscope. Despite the fact that microscope was used for only magnification and observation of detailed images at the beginning, it has rapid progress in historical record. After solving problems and contradictions about propagation of light and diffraction limit by using Fresnel principle and Abbe theorem in 1800's, a myriad of new methods were developed. Spectrophotometry, ellipsometry, optical profilometry and Raman spectroscopy are some of these methods. They can be categorized according to using of properties of light such that ellipsometry uses the polarization property of light whereas Raman spectroscopy uses scattering property.

The developments on thin film coating technology are increasing day by day. They have large usage area and their quality are determined via some parameters which is called as thin film assessment. Optical characterization techniques can be used in this process. It contributes to determination of thickness, refractive index distribution, surface profiling and uniformity of the thin film.

The coating or buffer of fiber optics protects the optical fiber from the chemical and mechanical damages (Wojcik et al., 2006) since reliability and expected lifetime are essential parameters for optical fibers (Severin et al., 2007). It also contributes to modulating the light wave when exposed to a certain measure. By using this opinion, thin film coated optical fibers started to used as a sensor (Renoirt et al., 2013). When the measurand is changed, the sensitivity type of sensor changes (Ekici, 2016). In this way, it can be used as temperature sensor, humidity sensor, acoustic sensor etc. In order to obtain better sensitivity beyond the diffraction limits, the physical properties of optical fiber must be known and the thickness is one of them.

Optical characterization methods usually depend on the interferometric techniques. Although they are effective methods for thin film assessment, they have some difficulties on curved surfaces because of using reflected waves for determination. Therefore, new methods such as diffraction techniques proposed to used on curved surfaces (Ekici and Dinleyici, 2017).

1.2. Review of the Thesis

This thesis is aimed at the sub-wavelength thickness estimation of dielectric nano-scale films on curved surfaces by using near field diffraction method beyond the diffraction limits. Various light sources have been achieved to improve resolution up to one tenth of wavelength. Furthermore, the higher order components of diffracted waves can be used

by studying at very close proximity to the sensor array. In this way, not only the sharp and rapid changes in the diffraction pattern have been obtained but also all k-components can be found on diffraction pattern.

The chapters of thesis are:

- Chapter 2 starts with discussion about scalar diffraction theory. The classical and near field Kirchoff diffraction formula were revisited. Then, diffraction limits were evaluated around the Point Spread Function (PSF) perspective since the assertion of thesis is that sub-wavelength thicknesses can be estimated by exploiting these techniques. The purpose is to prove that diffraction limit criteria such as Abbe, Rayleigh etc. can be stretched. The final part of this chapter is about the modal analysis of optical fiber because of the fact that structured light has a key role to exceed the diffraction limits. The theory and mathematical preliminaries were given for the next sections.
- Chapter 3 introduce a mathematical model based on the near field diffraction method for cylindrical phase objects by using various structured lights.
- Chapter 4 begins with the assembly procedure. Then, the generation of structured light and sensing process are explained. The results were obtained for various structured lights and coatings. Also, the comparisons with SEM results can be found in this chapter.
- Chapter 5 is about the conclusion and future works. The interpretations were made for different sources types and conventional methods. The effect of structured light defined with reasons and comparisons. Since the thickness of thin films has importance for sensor technologies especially Surface Plasmon Resonance (SPR) sensors, the route of the future works were plotted.

CHAPTER 2

THEORY AND MATHEMATICAL PRELIMINARIES

In this chapter, scalar diffraction theory, limits of diffraction and modal analysis of optical fibers are examined. The aim of this chapter is preparation to obtaining diffraction model of cylindrical phase objects by evaluation around diffraction limits with some conclusions.

2.1. Diffraction

Diffraction can be described as the propagation of light through the objects or apertures. It should be examined into two perspectives: vectorial and scalar. Scalar approach means that the polarization of wave is ignored and is generally used because of simplicity. There are two conditions must be satisfied about the transition to scalar theory: (1) Diffraction field must be calculated larger than sub-wavelength distance from the aperture (Kowarz, 1995) and (2) The aperture must be larger than wavelength (Goodman, 1996). However, the classical scalar diffraction theory is not suitable to find the field generated by sub-wavelength object, it can account for propagation of field for distances away from the object (Makris and Psaltis, 2011). Therefore, there is needed to describe diffraction in sub-wavelength propagation distances. It can be possible with that dipoles are placed on wave-front, on the contrary to conventional Huygens' Fresnel principle. In this way, the exact solution obtained by that non-paraxial regime behaviour (Andrews, 1951), backward parts of waves by using dipoles (Miller, 1991) and evanescent waves can take into account.

2.1.1. Kirchoff Diffraction Theory

The beginning of diffraction theory dates back to Huygens' principle. According to Huygens' idea, every point of wave-front serves as source of secondary disturbance and new wave-front is the summation of these disturbances (Huygens, 1912). The missing part about this theory is that there is no information about frequency or wavelength of

the wave. Therefore, the formula developed by Fresnel at a later time by adding that secondary wavelets which has information about being same frequency. In this way the Huygens'-Fresnel principle obtained by combination of two ideas.

Let a point source make radiation at point P_0 and produced spherical monochromatic wave-front with radius r_0 represented by S. The contribution to the light disturbance $dU(P)$ because of the element dS at Q by omitting time factor $\exp(-i\omega t)$ can be defined as (Born and Wolf, 1999)

$$dU(P) = K(\chi) \frac{A \exp(ikr_0)}{r_0} \frac{\exp(iks)}{s} dS \quad (2.1)$$

where A and $K(\chi)$ are amplitude and inclination factor. The inclination factor includes the diffraction angle between the normal at point Q and QP line and describes the amplitude variation with respect to the direction.

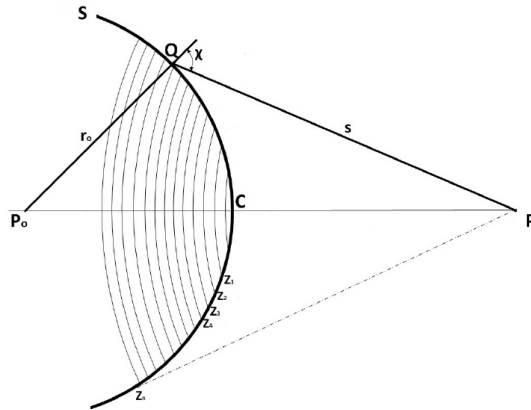


Figure 2.1. Fresnel Zones

Because of shortcomings of Huygens' Fresnel principle especially about the determination of inclination factor, Gustav Kirchoff derived a more rigorous integral theorem which depends on the solution of the homogeneous differential wave equation. The solution of wave equation is implemented with the help of Green's theorem.

Let U and G be any two complex-valued position functions, S be closed surface and V be a volume inside closed surface S. If U, G, and their first and second partial derivatives are single-valued and continuous within and on S, then we have

$$\int \int \int_V (U \nabla^2 G - G \nabla^2 U) dV = \int \int_S \left(U \frac{\partial G}{\partial n} - G \frac{\partial U}{\partial n} \right) \quad (2.2)$$

where $\partial/\partial n$ denotes partial derivative in the outward direction normal to S.

It is seen that U is a solution of Helmholtz equation. Then, a reduction can be done in Equation 2.2 by choosing auxiliary function G which satisfies the Helmholtz equation:

$$(\nabla^2 + k^2) \begin{pmatrix} U \\ G \end{pmatrix} = 0 \quad (2.3)$$

$$\int \int_S \left(U \frac{\partial G}{\partial n} - G \frac{\partial U}{\partial n} \right) = 0 \quad (2.4)$$

The auxiliary function G contributes to examine the disturbance at point P . Therefore, it can be defined as a probe. Suppose that G was chosen $\exp(iks/s)$ where s denotes the distance from P to the arbitrary point (x,y,z) and it can be seen that singularity at $s=0$. In Equation (2.4), it was stated that both U and G satisfies homogeneous Helmholtz Equation. Therefore, it can not be any source inside closed surface S and also P must be excluded from the domain of integration with the help of small spherical surface S_ϵ , of radius ϵ , inserted about the point P . At the end the integral formula of Kirchoff-Helmholtz can be obtained as

$$U(P) = \frac{1}{4\pi} \int \int_S \left\{ \frac{\partial U}{\partial n} \left(\frac{\exp(iks)}{s} \right) - U \frac{\partial}{\partial n} \left(\frac{\exp(iks)}{s} \right) \right\} dS \quad (2.5)$$

This equation has key role in the development of scalar diffraction theory. The field at any point can be expressed in terms of the boundary values thanks to this integral formula. Besides, the formula derived for the strictly monochromatic wave.

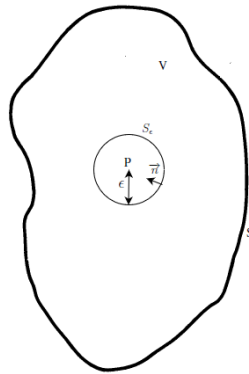


Figure 2.2. Surface of integration

Now, let's examine the diffraction problem by a planar screen by using Kirchoff integral theorem. Consider a point source at P_0 makes radiation through the planar aperture and the disturbance point P is investigated. If the Kirchoff integral is used to find disturbance, the integration can be divided 3 parts:(1) the opening part(A) (2) the closed

or non illuminated part B and (3) the closed surface C which has a centre at P with large sphere of radius R . Then, the Kirchoff integral can be expressed as:

$$U(P) = \frac{1}{4\pi} \left\{ \int \int_A + \int \int_B + \int \int_C \right\} \left\{ \frac{\partial U}{\partial n} \left(\frac{\exp(iks)}{s} \right) - U \frac{\partial}{\partial n} \left(\frac{\exp(iks)}{s} \right) \right\} dS \quad (2.6)$$

Kirchoff set the boundary conditions by making two assumptions: (1) the field distribution U and its derivative $\partial U/\partial n$ are equal to each other on the boundary A where U and $\partial U/\partial n$ represent incident field and diffracted field respectively. (2) the field distribution U and its derivative $\partial U/\partial n$ are zero on the region B . Hence, the Kirchoff boundary conditions can be written as (see Figure 2.3(a)):

$$U = U^{(i)}, \quad \frac{\partial U}{\partial n} = \frac{\partial U^{(i)}}{\partial n} \quad \text{on } A \quad (2.7)$$

$$U = 0, \quad \frac{\partial U}{\partial n} = 0 \quad \text{on } B \quad (2.8)$$

where

$$U^{(i)} = \frac{A \exp(ikr)}{r}, \quad \frac{\partial U^{(i)}}{\partial n} = \frac{A \exp(ikr)}{r} \left[ik - \frac{1}{r} \right] \cos(n, r) \quad (2.9)$$

where $U^{(i)}$, $\cos(n, r)$, A are incident field, angle (see Figure 2.3(b)) and constant individually.

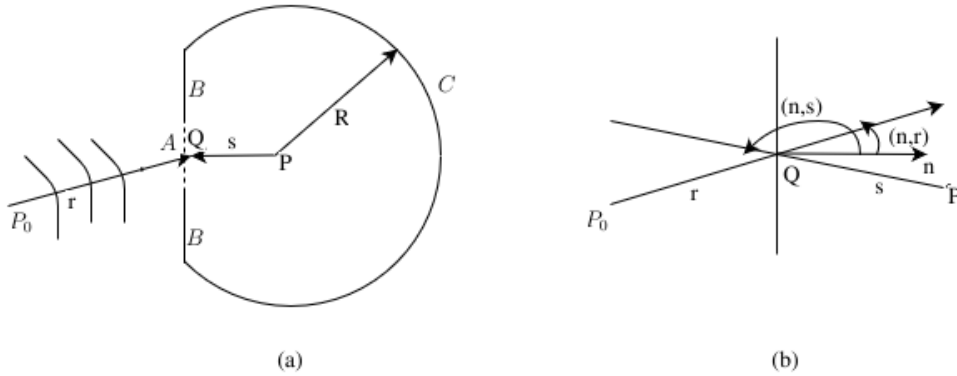


Figure 2.3. Illustration of integration surface(a) and boundary conditions

The contributions to the field U by the portion A and B were explained. Now, the contribution of portion C will be examined. It can be seen that the integral of C will be zero, if the radius of closed surface R be sufficiently large. However, there is a contradiction between the definition of monochromatic wave and vanishing of contribution of C

because monochromatic wave is found all times and space from its definition. This claim can be avoided by thinking that it is physically impossible to produce monochromatic wave. Therefore, substituting into Equation (2.11) and neglecting the terms $1/r$ and $1/s$ by comparing to k , the field becomes:

$$U(P) = -\frac{i}{2\lambda} \int \int_A \frac{\exp(ik(r+s))}{rs} [\cos(n, r) - \cos(n, s)] dS \quad (2.10)$$

This formula is called as Fresnel-Kirchhoff diffraction formula. The minus sign represents the partial derivative $\partial/\partial n$ in the inward normal direction. However, the sign variation does not affect the measurable quantity intensity since it is equal to square of field.

The propagation of wave-front might be expressed by choosing new boundaries. In this way, the explicit formula can be derived for the inclination factor $K(\chi)$. Let us assume that W is a portion of incident wave-front and filled the aperture approximately at boundary. On W , r_o and n are in the reverse direction so $\cos(n, r_o) = -1$ and diffraction angle is $\chi = (r_o, s)$. Then, the field U becomes:

$$U(P) = -\frac{i}{2\lambda} \frac{A \exp(ikr_o)}{r_o} \int \int_W \frac{\exp(iks)}{s} (1 + \cos(\chi)) dS \quad (2.11)$$

If the contribution of dW is written:

$$\frac{i}{2\lambda} \frac{A \exp(ikr_o)}{r_o} \frac{\exp(iks)}{s} (1 + \cos(\chi)) dS \quad (2.12)$$

and compared with Equation (2.1), the explicit formula for inclination factor is derived:

$$K(\chi) = -\frac{i}{2\lambda} (1 + \cos(\chi)) \quad (2.13)$$

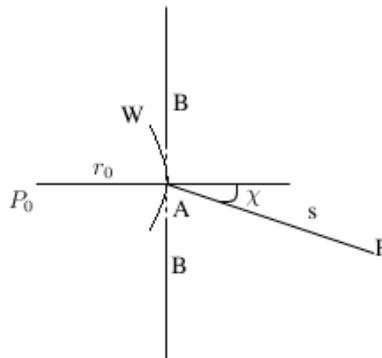


Figure 2.4. Illustration of new boundaries

The classical Huygens-Fresnel diffraction formula was derived up to now. However, it does not include near field terms, backward parts of the wave and it is not suitable for non paraxial regimes or sub-wavelength distances. Therefore, there is a need for a correction on the classical formula. It can be realized by an exact solution. Now, we derive a general form for the Kirchoff theorem which includes both monochromatic and non monochromatic waves.

Let V be a solution of the time dependent wave equation and its Fourier integrals can be expressed as

$$V(x, y, z, t) = \frac{1}{\sqrt{2\pi}} \int_{-\infty}^{\infty} U(x, y, z) \exp(-i\omega t) d\omega \quad (2.14)$$

$$U(x, y, z, t) = \frac{1}{\sqrt{2\pi}} \int_{-\infty}^{\infty} V(x, y, z, t) \exp(-i\omega t) dt \quad (2.15)$$

If $V(x, y, z, t)$ satisfies the regularity conditions inside and on a closed surface S , Kirchoff's theorem can be applicable to both $V(x, y, z, t)$ and its Fourier components $U(x, y, z)$. Therefore, it can be written as:

$$U(P) = \frac{1}{4\pi} \int \int_S \left\{ \frac{\partial U}{\partial n} \left(\frac{\exp(iks)}{s} \right) - U \frac{\partial}{\partial n} \left(\frac{\exp(iks)}{s} \right) \right\} dS \quad (2.16)$$

When Equation (2.8) is written in Equation (2.6) by changing the integration order and writing $k = \omega/c$, the equation becomes

$$\begin{aligned} V(P, t) &= \frac{1}{4\pi} \int \int_S dS \frac{1}{\sqrt{2\pi}} \int_{-\infty}^{\infty} \left\{ U \frac{\partial}{\partial n} \left(\frac{\exp(-i\omega(t - s/c))}{s} \right) - \right. \\ &\quad \left. \frac{\exp(-i\omega(t - s/c))}{s} \frac{\partial U}{\partial n} \right\} d\omega \\ &= \frac{1}{4\pi} \int \int_S dS \frac{1}{\sqrt{2\pi}} \int_{-\infty}^{\infty} \left\{ U \left\{ \frac{\partial}{\partial n} \left(\frac{1}{s} \right) + \frac{i\omega}{sc} \frac{\partial s}{\partial n} \right\} - \right. \\ &\quad \left. \frac{\exp(-i\omega(t - s/c))}{s} \frac{\partial U}{\partial n} \right\} d\omega \end{aligned} \quad (2.17)$$

or

$$V(P, t) = \frac{1}{4\pi} \int \int_S \left\{ [V] \frac{\partial}{\partial n} \left(\frac{1}{s} \right) - \frac{1}{cs} \frac{\partial s}{\partial n} \left[\frac{\partial V}{\partial t} \right] - \frac{1}{s} \left[\frac{\partial V}{\partial n} \right] \right\} dS \quad (2.18)$$

where $[]$ denotes retarded values.

The general solution was given in Equation (2.18). This is also called the near field or modified Huygens-Fresnel formula because of the fact that it includes near field terms. The integrand can be written as:

$$\frac{[V]}{4\pi s} \left\{ ik(1 + \cos \theta) + \frac{\cos \theta}{s} \right\} \quad (2.19)$$

where $\frac{\partial s}{\partial n} = -\cos\theta$. In classical Huygens-Fresnel diffraction formula, the third term is omitted since $s \gg \lambda$. However, the third term has importance in near field regime. Therefore, it called as near field term. This is the exact solution and valid for all distances. Besides, this formula corresponds of using dipoles instead of point sources on the contrary to conventional formula.

Consequently, the exact Huygens-Fresnel equation might be taken into consideration when it is desired to determine the field distribution of the spherical wave front at any point. Since it can be used to tracing of wave-front, it can be suitable for diffraction problem from phase objects.

2.2. Diffraction Limit

Spatial resolution is a measure the ability of how closely point-like objects can be distinguished. However, this ability has strong relation with the wavelength of light. The wavelength of light limits the resolution. This situation called as diffraction limit or barrier. Before the development on near field optics, the diffraction limit was defined $\lambda/2$ as a strict criteria .

The point spread function (PSF) is the measurement ability of resolving power. PSF definition depends on scalar theory and paraxial approximation. A classical image formation system (Enderlain, 2000) is given in Figure 2.5.

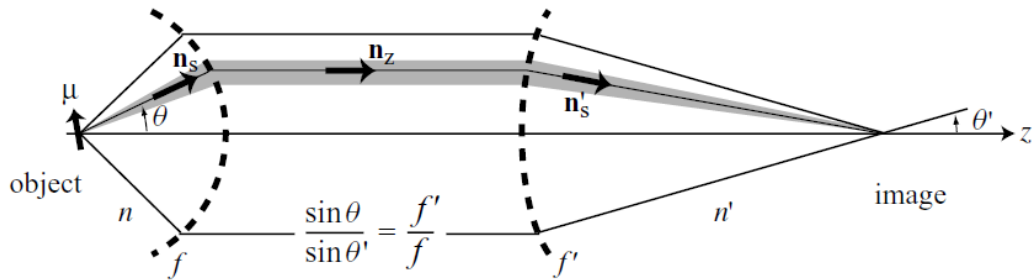


Figure 2.5. A system used for the calculation of PSF (Novotny and Hecht, 2012)

An electric dipole is located at the objective lens with focal length f . The first lens collimates the rays which comes from the dipole whereas second lens with focal length f' focuses them. Besides, there some assumptions that distance between dipole and lens is greater than the wavelength of the emitted light, evanescent waves can not taken into account and the dipole aligned with x-axis ($\mu = \mu_x \mathbf{n}_x$) surrounded by homogeneous

medium with refractive index n . The electric field at a point \mathbf{r} created by an electric dipole at \mathbf{r}_0 with electric dipole moment $\boldsymbol{\mu}$ which represents the object can be defined as

$$\mathbf{E}(\mathbf{r}) = \frac{\omega^2}{\epsilon_0 c^2} \overleftrightarrow{\mathbf{G}}(\mathbf{r}, \mathbf{r}_0) \cdot \boldsymbol{\mu} \quad (2.20)$$

where $\overleftrightarrow{\mathbf{G}}(\mathbf{r}, \mathbf{r}_0)$ is dyadic Green function.

The far field $\overleftrightarrow{\mathbf{G}}$ in source free medium can be written in spherical coordinates

$$\overleftrightarrow{\mathbf{G}}_f(\mathbf{r}, 0) = \frac{\exp(ikr)}{4\pi r} \times \begin{bmatrix} 1 - \cos^2 \phi \sin^2 \theta & -\sin \phi \cos \phi \sin^2 \theta & -\cos \phi \sin \theta \cos \theta \\ -\sin \phi \cos \phi \sin^2 \theta & 1 - \sin^2 \phi \sin^2 \theta & -\sin \phi \sin \theta \cos \theta \\ -\cos \phi \sin \theta \cos \theta & -\sin \phi \sin \theta \cos \theta & \sin^2 \theta \end{bmatrix} \cdot \boldsymbol{\mu} \quad (2.21)$$

After two refractions from the lenses, the field becomes

$$\mathbf{E}_f^x(\theta, \phi) = -\frac{\omega^2 \mu_x \exp(ikf)}{\epsilon_0 c^2} \frac{1}{8\pi f} \times \begin{bmatrix} (1 + \cos \theta \cos \theta') - (1 - \cos \theta \cos \theta' \cos 2\phi) \\ -(1 - \cos \theta \cos \theta' \cos 2\phi) \\ 2 \cos \theta \sin \theta' \cos \phi \end{bmatrix} \sqrt{\frac{n \cos \theta}{n \cos \theta'}} \quad (2.22)$$

where $\sin \theta' = (\frac{f}{f'} \sin \theta)$ and $\cos \theta' = g(\theta) = \sqrt{1 - (f/f')^2 \sin^2 \theta}$. This is the x component of the electric field. The superposition can be applied with other components and total field becomes

$$\mathbf{E}_f(\theta, \phi) = \mathbf{E}_f^x + \mathbf{E}_f^y + \mathbf{E}_f^z \quad (2.23)$$

As a result the final electric field can be written as (see Appendix D and section 3.5. in (Novotny and Hecht, 2012)):

$$\mathbf{E}(\rho, \varphi, z) = \frac{\omega^2}{\epsilon_0 c^2} \overleftrightarrow{\mathbf{G}}_{PSF}(\rho, \varphi, z) \cdot \boldsymbol{\mu} \quad (2.24)$$

where the dyadic point-spread function is given by

$$\overleftrightarrow{\mathbf{G}}_{PSF} = \frac{k'}{8\pi i} \frac{f}{f'} \exp(i(kf - k'f')) \begin{bmatrix} (I_{00}^{\sim} + I_{02}^{\sim} \cos 2\varphi) & I_{01}^{\sim} \sin 2\varphi & -2iI_{01}^{\sim} \cos \varphi \\ I_{02}^{\sim} \sin 2\varphi & (I_{00}^{\sim} - I_{02}^{\sim} \cos 2\varphi) & -2iI_{01}^{\sim} \cos \varphi \\ 0 & 0 & 0 \end{bmatrix} \quad (2.25)$$

and the integrals are

$$I_{00}^{\sim}(\rho, z) = \int_0^{\theta_{max}} \sqrt{\cos \theta} \sin \theta (1 + \cos \theta) J_0(k' \rho \sin(\theta) f/f') \times \exp(ik'z[1 - 1/2(f/f')^2 \sin^2 \theta]) d\theta \quad (2.26)$$

$$I_{01}^{\sim}(\rho, z) = \int_0^{\theta_{max}} \sqrt{\cos \theta} \sin^2 \theta J_1(k' \rho \sin(\theta) f/f') \times \exp(ik'z[1 - 1/2(f/f')^2 \sin^2 \theta]) d\theta \quad (2.27)$$

$$I_{02}^{\sim}(\rho, z) = \int_0^{\theta_{max}} \sqrt{\cos \theta} \sin \theta (1 - \cos \theta) J_0(k' \rho \sin(\theta) f/f') \times \exp(ik'z[1 - 1/2(f/f')^2 \sin^2 \theta]) d\theta \quad (2.28)$$

Since optical detectors can measure the intensity of field, PSF represented by $|\mathbf{E}^2|$. If assumptions are made that the lenses have low numerical aperture and θ_{max} is sufficiently small, the approximations become $\cos \theta \approx 1$ and $\sin \theta \approx \theta$. Furthermore, at $z = 0$ and $\vartheta = \pi/2$, the exponential terms equal to 1 and Bessel second kind J_2 goes to zero. Therefore, I_{02}^{\sim} can be ignored. Then I_{00}^{\sim} is left and integrated analytically

$$\int x J_0(x) dx = x J_1(x) \quad (2.29)$$

Consequently, the paraxial PSF can be found for a dipole along the x-axis becomes

$$\lim_{\theta_{max} < \pi/2} |\mathbf{E}(x, y, z = 0)|^2 = \frac{\pi^4}{\epsilon_0^2 n n'} \frac{\mu_x^2}{\lambda^6} \frac{NA}{M^2} \left[2 \frac{J_1(2\pi\tilde{\rho})}{\tilde{2}\pi\rho} \right]^2, \quad \tilde{\rho} = \frac{NA\rho}{M\lambda} \quad (2.30)$$

Besides, the PSF along and perpendicular to the optical axis can be found as:

$$\lim_{\theta_{max} < \pi/2} |\mathbf{E}(x = 0, y = 0, z)|^2 = \frac{\pi^4}{\epsilon_0^2 n n'} \frac{\mu_x^2}{\lambda^6} \frac{NA}{M^2} \left[2 \frac{\sin(\pi\tilde{z})}{\pi\tilde{z}} \right]^2, \quad \tilde{z} = \frac{NA^2 z}{2n'M^2\lambda} \quad (2.31)$$

$$\lim_{\theta_{max} < \pi/2} |\mathbf{E}(x, y, z = 0)|^2 = \frac{\pi^4}{\epsilon_0^2 n n'} \frac{\mu_x^2}{\lambda^6} \frac{NA}{M^2} \left[2 \frac{J_1(2\pi\tilde{\rho})}{\tilde{2}\pi\rho} \right]^2, \quad \tilde{\rho} = \frac{NA\rho}{M\lambda} \quad (2.32)$$

where NA is numerical aperture and M is magnification. It can be seen that the orientation of dipoles affect the PSF. Also, the total PSF of system can be defined as the product of the PSF of excitation and PSF of detection.

The PSF gives information about how the point source spreads. It can easily concluded that the narrower PSF implies a point and so better resolution. A point defined by Dirac delta function (δ) in space and has infinite spectrum in k-domain. Since the point source is theoretical and the images in nature have finite bandwidth, the whole information about image can not be obtained.

If two point sources get closer to each other, their point spread functions start to overlap at a point. It means that two point sources become indistinguishable. Let us assumed that two point-like object, in a noise free medium, separated from each other with distance:

$$\Delta r = (\Delta x^2 + \Delta y^2)^{1/2} \quad (2.33)$$

and the bandwidth of spatial frequencies

$$\Delta k = (\Delta k_x^2 + \Delta k_y^2)^{1/2} \quad (2.34)$$

According to the consequence Fourier transform relationship, called uncertainty relations, between $\vec{E}(\vec{r}, z = 0)$ and $\vec{E}(\vec{k}, z = 0)$ (Carminati, Carminati)

$$\Delta k \Delta r \geq 1 \quad (2.35)$$

It can be concluded that if Δk is infinitely large, there is no diffraction limit. If the evanescent waves are not included, the upper bound of Δk can be found by the transverse wavenumber $k = (w/c)n = (2\pi/\lambda)n$. Therefore, using the uncertainty relation

$$K \Delta r_{min} = \frac{\lambda}{2\pi n} \quad (2.36)$$

or

$$\Delta r_{min} = \frac{\lambda}{2\pi NA} \quad (2.37)$$

where n is the refractive index of medium and NA is numerical aperture.

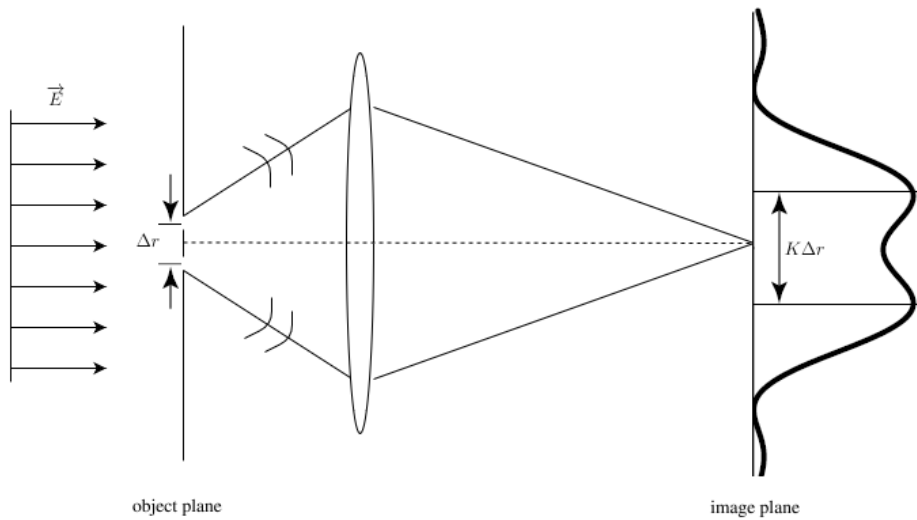


Figure 2.6. Illustration of diffraction limits of two point sources separated from each other Δr

In 1874, Abbe described diffraction limit over two dipole. The minimum distance between point spread functions of two dipoles $K \Delta r$ defined as the intersection of maximum of one point-spread function with first minimum of the second point-spread function. According to the Abbe's diffraction limit formula:

$$\Delta r_{min} = \frac{\lambda}{2NA} \quad (2.38)$$

If Equation (2.37) is compared with Equation (2.38), there is difference in denominator. The reason is about the definition of diffraction limit. Abbe implemented this formula according to paraxial approximation and parallel dipoles which are perpendicular to optical axis and have equal strength. Besides, Rayleigh modified Abbe's formula. The Rayleigh criteria definition is made over Airy disc. Therefore, it is the measure of distinguishable of two Airy discs and the minimum distance defined as:

$$\Delta r_{min} = 0.61 \frac{\lambda}{NA} \quad (2.39)$$

2.3. Structured Lightwave Generation

The propagation of light inside an optical fiber can be analysed with the Maxwell equations (Harrington, 2001). In zero conductivity situation, the vectorial relationships can be represented in terms of electric field \mathbf{E} , magnetic field \mathbf{H} , electric flux density \mathbf{D} and magnetic flux density \mathbf{B} . In a source free medium, the Maxwell equations and constitutive relations are:

$$\nabla \times \mathbf{E} = -\frac{\partial \mathbf{B}}{\partial t} \quad (2.40)$$

$$\nabla \times \mathbf{H} = \frac{\partial \mathbf{D}}{\partial t} \quad (2.41)$$

$$\nabla \times \mathbf{D} = 0 \quad (2.42)$$

$$\nabla \times \mathbf{B} = 0 \quad (2.43)$$

$$\mathbf{D} = \epsilon \mathbf{E} \quad (2.44)$$

$$\mathbf{B} = \mu \mathbf{H} \quad (2.45)$$

where ∇ , ϵ and μ are vector operator, dielectric permittivity and magnetic permeability of the medium respectively. Substituting for \mathbf{D} and \mathbf{B} , taking the curl of Equation (2.40) and (2.41) and using mathematical identities, the wave equation is obtained both \mathbf{E} and \mathbf{H} :

$$\nabla^2 \mathbf{E} = \epsilon \mu \frac{\partial^2 \mathbf{E}}{\partial t^2} \quad (2.46)$$

$$\nabla^2 \mathbf{H} = \epsilon \mu \frac{\partial^2 \mathbf{H}}{\partial t^2} \quad (2.47)$$

If the wave equation is solved with appropriate boundary conditions, the propagation of light inside an optical fiber can be examined. Besides, the analysis is made in

cylindrical coordinate system since optical fibers have cylindrical structures. Then, the wave equation becomes for \mathbf{E} :

$$\frac{\partial^2 \mathbf{E}}{\partial r^2} + \frac{1}{r} \frac{\partial \mathbf{E}}{\partial r} + \frac{1}{r^2} \frac{\partial^2 \mathbf{E}}{\partial \phi^2} + \frac{\partial^2 \mathbf{E}}{\partial z^2} = \epsilon \mu \frac{\partial^2 \mathbf{E}}{\partial t^2} \quad (2.48)$$

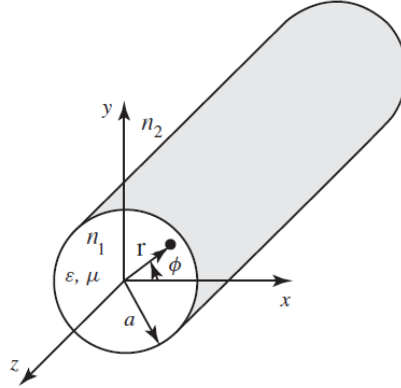


Figure 2.7. Cylindrical geometry cross section (Balanis, 2012)

There are six field components for \mathbf{E} and \mathbf{B} and these components are not independent from each other. Therefore, two components are chosen and the others are expressed in terms of them. In the optical fibers, the longitudinal components \mathbf{E}_z and \mathbf{H}_z are taken base components and the wave equation is solved for these two components. Then transverse field components are expressed in terms of these two components by substitution of the longitudinal components in the Maxwell's equations. The transverse field components are:

$$E_r = -\frac{i}{q^2} \left\{ \beta \frac{\partial E_z}{\partial r} + \frac{\mu \omega}{r} \frac{\partial H_z}{\partial \phi} \right\} \quad (2.49)$$

$$E_\phi = -\frac{i}{q^2} \left\{ \frac{\beta}{r} \frac{\partial E_z}{\partial \phi} - \mu \omega \frac{\partial H_z}{\partial r} \right\} \quad (2.50)$$

$$H_r = -\frac{i}{q^2} \left\{ \beta \frac{\partial H_z}{\partial r} - \frac{\epsilon \omega}{r} \frac{\partial E_z}{\partial \phi} \right\} \quad (2.51)$$

$$H_\phi = -\frac{i}{q^2} \left\{ \frac{\beta}{r} \frac{\partial H_z}{\partial \phi} + \epsilon \omega \frac{\partial E_z}{\partial r} \right\} \quad (2.52)$$

where β is the propagation constant and $q^2 = \omega^2 \mu \epsilon - \beta^2$. Each components of \mathbf{E} and \mathbf{B} are scalar quantities. Therefore, the wave equation is solved for scalar function ψ where ψ is E_z or H_z . In this way, the wave equation can be written as:

$$\frac{\partial^2 \psi}{\partial r^2} + \frac{1}{r} \frac{\partial \psi}{\partial r} + \frac{1}{r^2} \frac{\partial^2 \psi}{\partial \phi^2} + \frac{\partial^2 \psi}{\partial z^2} = \epsilon \mu \frac{\partial^2 \psi}{\partial t^2} \quad (2.53)$$

The solution of Equation (2.53) can be obtained by using separation of variables method. Hence, the scalar function ψ is written as:

$$\psi = R(r)\Phi(\phi)Z(z)T(t) \quad (2.54)$$

Now let's examine four variable:

- If the fields are time harmonic field, then

$$\psi \sim \exp(i\omega t) \Rightarrow T(t) = \exp(i\omega t)$$

$$\frac{\partial}{\partial t} = i\omega, \quad \frac{\partial^2}{\partial t^2} = -\omega^2$$

- If the wave travels along the fiber axis which is +z-direction, then

$$\psi \sim \exp(-i\beta z) \Rightarrow Z(z) = \exp(-i\beta z)$$

$$\frac{\partial^2}{\partial z^2} = -\beta^2$$

- If wave motion is only azimuthal direction ϕ , the scalar function ψ is periodic in 2π

$$\psi \sim \exp(i\nu\phi) \Rightarrow \Phi(\phi) = \exp(-i\nu\phi)$$

$$\frac{\partial^2}{\partial \phi^2} = -\nu^2$$

where ν is an integer. Substituting these three variables into Equation (2.53), the wave equation becomes

$$\frac{d^2 R}{dr^2} + \frac{1}{r} \frac{dR}{dr} + \left\{ -\frac{\nu^2}{r^2} - \beta^2 + \omega^2 \mu \epsilon \right\} R = 0 \quad (2.55)$$

or

$$\frac{d^2 R}{dr^2} + \frac{1}{r} \frac{dR}{dr} + \left\{ q^2 - \frac{\nu^2}{r^2} \right\} R = 0 \quad (2.56)$$

This equation is called as Bessel equation and so the solutions of wave equation is Bessel functions.

The solution of Bessel equation depends on two variables q and ν . ν is integer and positive whereas q can be real, imaginary and complex. However, the choice of q has limitation by physical understanding.

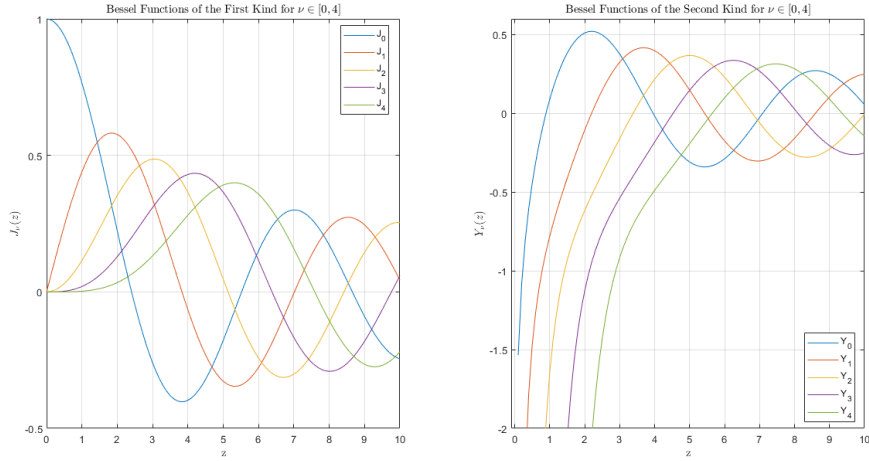


Figure 2.8. Bessel first kind and second kind functions

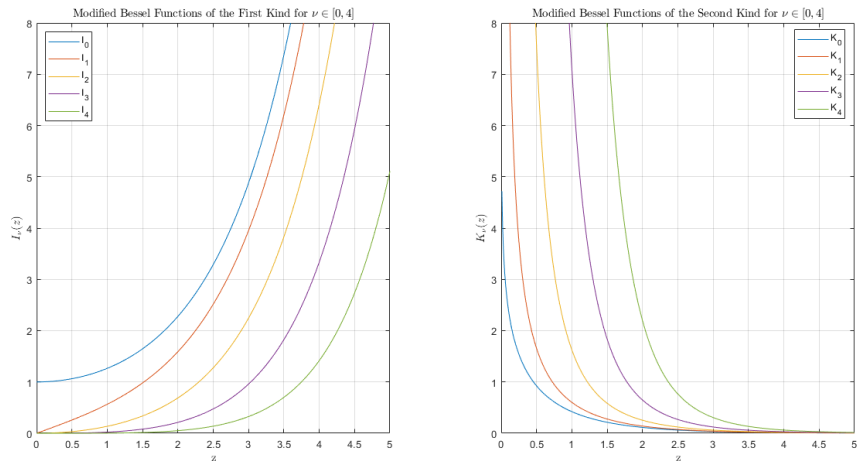


Figure 2.9. Modified Bessel first kind and second kind functions

If q is real, the solutions are Bessel first kind $J_\nu(qr)$ and Bessel second kind (Neumann) $Y_\nu(qr)$ functions. The parameters ν and qr define the order and argument of function respectively. If q is imaginary, the solutions are modified Bessel first kind $I_\nu(qr/i)$ and Bessel second kind $K_\nu(qr/i)$ functions. If q is complex the solutions are Hankel first kind $H_\nu(qr)$ and Hankel second kind $H_\nu(qr)$ functions. Hankel functions are used in examining lossy medium. However, the light propagation inside an optical fiber, the assumption is that the medium is lossless.

Now let us examine the Bessel first kind and Neumann functions for core and cladding. For the core, $r = 0$ corresponds to axis of fiber and the field strength has

finite value. Therefore, if Neumann function is chosen as a solution inside the core, it becomes inconsistent because of physical conditions. Hence, first kind Bessel functions is appropriate solution to describe the modal fields inside the core. For the cladding, the wave has decaying behaviour. It means that q must be imaginary and modified Bessel functions has to be used. For modified Bessel's functions of first kind, field increases with $r \rightarrow \infty$. However, it is not possible situation since field can not be shown increasing behaviour. Therefore, the correct solution for the cladding is modified Bessel function of second kind.

Consequently, the field distribution for the core and cladding can be defined as:

$$E_{z1} = AJ_\nu(ur) \exp(i\nu\phi - i\beta z + i\omega t), \quad r < a \quad (2.57)$$

$$H_{z1} = BJ_\nu(ur) \exp(i\nu\phi - i\beta z + i\omega t), \quad r < a \quad (2.58)$$

$$E_{z2} = CK_\nu(wr) \exp(i\nu\phi - i\beta z + i\omega t), \quad r > a \quad (2.59)$$

$$H_{z2} = DJ_\nu(wr) \exp(i\nu\phi - i\beta z + i\omega t), \quad r > a \quad (2.60)$$

where A,B,C,D are constants according to boundary conditions, β and β_1 is the wave number free space and core, a is the radius of core and $u^2 = \beta_1^2 - \beta^2$.

If the boundary conditions are applied, the characteristic equation of the modes can be obtained. The boundary conditions at $r = a$ can be given as:

$$E_{\phi 1} = E_{\phi 2}, \quad H_{\phi 1} = H_{\phi 2},$$

$$E_{z1} = E_{z2}, \quad H_{z1} = H_{z2},$$

The characteristic equation(or eigen value equation) of mode inside an optical fiber is(Ghatak):

$$\left\{ \frac{J'_\nu(ua)}{uJ_\nu(ua)} + \frac{K'_\nu(ua)}{uK_\nu(ua)} \right\} \left\{ \beta_1^2 \frac{J'_\nu(ua)}{uJ_\nu(ua)} + \beta_2^2 \frac{K'_\nu(ua)}{uK_\nu(ua)} \right\} = \frac{\beta^2 \nu}{a} \left\{ \frac{1}{u^2} + \frac{1}{w^2} \right\} \quad (2.61)$$

where $u^2 = w^2 \mu \epsilon_1 - \beta^2$, $w^2 = \beta^2 - w^2 \mu \epsilon_2$ and β is the modal propagation constant. For $\nu = 0$ the Equation 2.48 becomes

$$\left\{ \frac{J'_\nu(ua)}{uJ_\nu(ua)} + \frac{K'_\nu(ua)}{uK_\nu(ua)} \right\} \left\{ \beta_1^2 \frac{J'_\nu(ua)}{uJ_\nu(ua)} + \beta_2^2 \frac{K'_\nu(ua)}{uK_\nu(ua)} \right\} = 0 \quad (2.62)$$

If the first bracket is zero, we can find transverse electric modes. However, if the second bracket is zero, we can find transverse magnetic modes.

2.3.1. Modal Structured Lightwaves

In optical fibers, the cladding refractive index(n_2) is slightly smaller than the core refractive index(n_1). This difference can be defined with normalized index parameter(Δ)

$$\Delta = \frac{n_1^2 - n_2^2}{2n_1} \approx \frac{n_1 - n_2}{n_1} \quad (2.63)$$

Since $\Delta \ll 1$, an approximation can be used in the modal analysis of optical fiber. This approximation is called as weakly guiding approximation (Gloge, 1971). In weakly guiding fiber, all modes which have same V-number would degenerate. It means that these modes propagate with same phase variation. Therefore, the field distribution is the combination of these modes. These fields are called as linearly polarized (LP) modes and their orientation is not change through the cross-section plane. Their electric and magnetic fields occur in single cartesian directions in the transverse plane(linear polarization). Therefore, the LP modes are analysed by the assumption that field solutions are linearly polarized in the fiber transverse plane.

Let electric field has x-polarization and magnetic field y-polarization. The optical fiber behaviour under weak guidance is nearly plane wave where \mathbf{E} and \mathbf{H} are orthogonal and have very small longitudinal component (Buck, 2004)

$$\mathbf{E} = E_{x0}(r, \phi) \exp(-i\beta z) \hat{\mathbf{a}}_x \quad (2.64)$$

$$\mathbf{H} = E_{y0}(r, \phi) \exp(-i\beta z) \hat{\mathbf{a}}_y \quad (2.65)$$

Since wave equation can be separated into x,y and z components, we have

$$\nabla_t^2 E_{x1} + (n_1^2 k_0^2 - \beta^2) E_{x1} = 0, \quad r \leq a \quad (2.66)$$

$$\nabla_t^2 E_{x2} + (n_2^2 k_0^2 - \beta^2) E_{x2} = 0, \quad r \geq a \quad (2.67)$$

where $n_1^2 k_0^2 - \beta^2 = \beta_{t1}^2$ and $n_2^2 k_0^2 - \beta^2 = \beta_{t2}^2$. If we assume that transverse variation occurs in r and ϕ , wave equation becomes

$$\frac{\partial^2 E_x}{\partial r^2} + \frac{1}{r} \frac{\partial E_x}{\partial r} + \frac{1}{r^2} \frac{\partial^2 E_x}{\partial \phi^2} + \beta_t^2 E_x = 0 \quad (2.68)$$

and E_x can be expressed as discrete series of modes:

$$E_x = \sum_i R_i(r) \Phi_i(\phi) \exp(-i\beta_i z) \quad (2.69)$$

where each mode of E_x must be satisfy Equation (2.68). If E_x is expressed as a single mode $R\Phi \exp(-i\beta_i z)$ and substitute into Equation (2.68)

$$\frac{r^2}{R} \frac{d^2 R}{dr^2} + \frac{r}{R} \frac{dR}{dr} + r^2 \beta^2 = -\frac{1}{\Phi} \frac{d^2 \Phi}{d\phi^2} \quad (2.70)$$

Both side of Equation (2.70) depends on only one variable r or ϕ . Since r or ϕ are independent, each side of Equation (2.70) must be equal to constant. Let the constant is defined by l^2 . Then, Equation (2.70) can be divided into two equations:

$$\frac{d\Phi}{d\phi^2} + l^2\Phi = 0 \quad (2.71)$$

$$\frac{d^2R}{dr^2} + \frac{1}{r} \frac{dR}{dr} + \left[\beta_t^2 - \frac{l^2}{r^2} \right] \quad (2.72)$$

where $\beta_t^2 - \frac{l^2}{r^2} = \beta_r^2$ and $l/r = \beta_\phi$.

The solution of Equation (2.71) yields

$$\Phi(\phi) = \begin{cases} \cos(l\phi + \alpha) \\ \sin(l\phi + \alpha) \end{cases} \quad (2.73)$$

where α is a constant phase shift and l is an integer which is called as angular mode number of LP modes.

The solution of Equation (2.72) yields

$$R(r) = \begin{cases} AJ_l(\beta_t r) + A'N_l(\beta_t r), & \beta_t \text{ real} \\ CK_l(|\beta_t|r) + C'I_l(|\beta_t|r), & \beta_t \text{ imaginary} \end{cases} \quad (2.74)$$

where $A' = 0$ and $C' = 0$ because of reasons which are defined in section 2.3.

Now, normalized transverse phase and attenuation constants can be defined as, respectively:

$$u = \beta_{t1}a = a(n_1^2k_0^2 - \beta^2)^{1/2} \quad (2.75)$$

$$w = |\beta_{t2}|a = a(\beta^2 - n_2^2k_0^2)^{1/2} \quad (2.76)$$

The complete solution for E_x and H_x is obtained by using $\cos(l\phi)$ in Equation (2.73) and assuming $\alpha = 0$;

$$E_x = \begin{cases} AJ_l(ur/a) \cos(l\phi) \exp(-i\beta z), & r \leq a \\ CK_l(wr/a) \cos(l\phi) \exp(-i\beta z), & r \geq a \end{cases} \quad (2.77)$$

$$H_x = \begin{cases} BJ_l(ur/a) \cos(l\phi) \exp(-i\beta z), & r \leq a \\ DK_l(wr/a) \cos(l\phi) \exp(-i\beta z), & r \geq a \end{cases} \quad (2.78)$$

To find the coefficient, there is needed to apply boundary conditions at $r = a$.

$$E_{\phi 1} = E_{\phi 2} \quad (2.79)$$

$$H_{\phi 1} = H_{\phi 2} \quad (2.80)$$

$$n_1^2 E_{r1} = n_2^2 E_{r2} \quad (2.81)$$

$$\mu_1 H_{r1} = \mu_2 H_{r2} \quad (2.82)$$

Since $\mu_1 = \mu_2 = \mu_0$ radial components of \mathbf{H} are continuous. Furthermore, we assume $n_1 = n_2$ because of weakly guiding approximation. It means that $E_{r1} \approx E_{r2}$. Using continuity of \mathbf{E} and \mathbf{H} ,

$$E_{x1} \approx E_{x2} \quad (2.83)$$

$$H_{y1} \approx H_{y2} \quad (2.84)$$

Also setting $A = E_0$ and using boundary conditions

$$E_x = \begin{cases} E_0 J_l(ur/a) \cos(l\phi) \exp(-i\beta z), & r \leq a \\ E_0 [J_l(u)/K_l(w)] K_l(wr/a) \cos(l\phi) \exp(-i\beta z), & r \geq a \end{cases} \quad (2.85)$$

which is called as general electric field for LP modes.

CHAPTER 3

MATHEMATICAL MODEL

In this chapter, near field Huygens-Fresnel diffraction theory analysed for cylindrical phase objects with causes and effects. The mathematical models obtained not only different ray tracing methods but also different illumination sources.

3.1. Diffraction from Cylindrical Objects

The amplitude and phase of the wave are two parameters to observe the diffraction effects. Since the variations of phase is more sensitive than amplitude, Fresnel diffraction becomes applicable. The phase change can be created by two ways depending on the object. If you have transparent object, the phase of wave can be changed by the sharp variation of thickness or refractive index of the object. These variations strongly affect the optical path length of wave and so the phase shows quick changes (Tavassoly et al., 2001). In this way, this feature can be exploited to measure refractive index, optical path length, thickness as an optical sensor.

While the diffraction effects are analyzing, the intensity pattern is affected by not only variations of refractive index and thickness but also the by illuminating source of phase object (Saxena, Eluru, and Gorthi, Saxena et al.). The using of various types sources means that the PSF of system is changed. Since the major changes on intensity pattern occurred by the contribution of sharp variations, the illumination of these variation regions with narrower PSF source provides the measurements of small refractive index or nano-scale thickness changes. Therefore, structured light modes can be chosen for sensitive measurements.

The Huygens-Fresnel principle can be modelled by wave-front tracing (Volpe et al., 2018). The wave-front is considered as an array of dipoles. The emitting wavelets from wave-front interfere with each other and the diffraction pattern occurs. Since every dipole can be represented by a ray, it can be called as ray-trace diffraction (Mahan et al., 2018).

The diffraction limit, was mentioned in section 2.2, is not a strict criteria. It can be stretched by using near field terms such as evanescent waves, dealing with an elementary

source as electric dipole or changing illumination source. Optical characterization can be made beyond diffraction limits thanks to them. In this way, the coated materials whose thicknesses are smaller than the half of wavelength can be measured. In our mathematical model, the diffraction limit examined by using electric dipoles on the wave-front, using near field or taking higher order terms by studying at very short distances and structured light sources to change the total PSF.

3.1.1. Plane Wave

In this part, the cylindrical phase object (fiber optic) is examined by the illumination of plane wave. Wave-front is discretized and every dipole over the wave-front represented by a ray. During the propagation, every ray is traced. After the finding of phase variations, near field Huygens-Fresnel principle is used to find disturbance on the screen. The ray tracing method is examined both paraxial and exact.

3.1.1.1. Paraxial Ray Tracing

The generated plane wave is sent to the coated fiber optic. In the figure, a is the radius of core, b is the radius cladding and the c is the coating diameter. The rays are traced up to x' plane and find the phase variations. After obtaining wave-front at x' , scalar diffraction integral is evaluated and the intensity pattern on the screen can be obtained. The applied field at X plane can be defined as

$$U(x, 0, z) = A(x) \exp(ikz) \quad (3.1)$$

In order to express the field point by point at x' plane, optical path lengths for every rays have to be defined. Therefore phase variations can be defined as (Sabatyan and Tavassoly, 2007):

$$\begin{aligned} \phi_1 = 2k[n_a(c - \sqrt{c^2 - x'^2}) + n_s(\sqrt{c^2 - x'^2} - \sqrt{b^2 - x'^2}) + \\ n_{cl}(\sqrt{b^2 - x'^2} - \sqrt{a^2 - x'^2}) + n_{co}\sqrt{a^2 - x'^2}], \quad |x'| < a \end{aligned} \quad (3.2)$$

$$\begin{aligned} \phi_2 = 2k[n_a(c - \sqrt{c^2 - x'^2}) + n_s(\sqrt{c^2 - x'^2} - \sqrt{b^2 - x'^2}) + \\ + n_{cl}\sqrt{b^2 - x'^2}], \quad b < |x'| < a \end{aligned} \quad (3.3)$$

$$\phi_3 = 2k[n_a(c - \sqrt{c^2 - x'^2}) + n_s\sqrt{b^2 - x'^2}], \quad b < |x'| < c \quad (3.4)$$

$$\phi_4 = 2kn_a c, \quad |x'| > c \quad (3.5)$$

where n_a, n_s, n_{cl}, n_{co} , and k are the refractive indices of the air, the coating, the cladding, the core and the wave number, respectively.

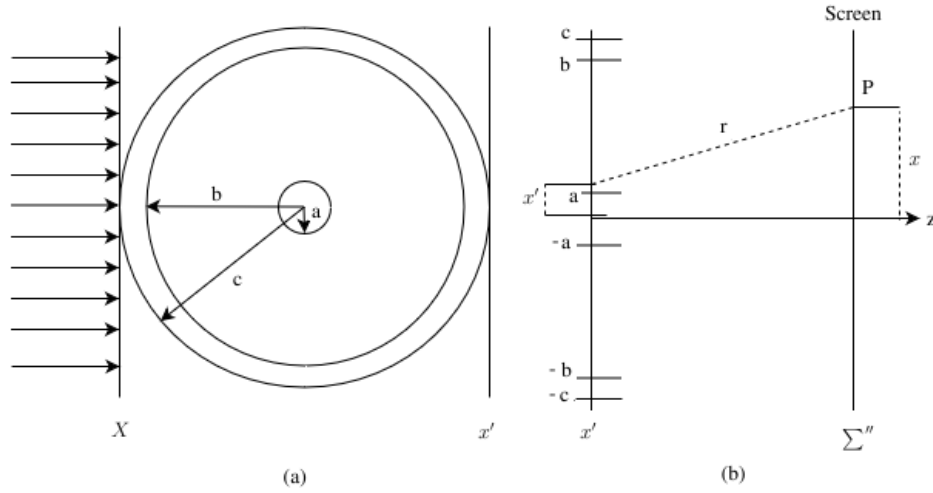


Figure 3.1. (a) Plane wave passing through cylindrical object, (b) Diffraction from cylindrical object

Denoting

$$\phi_a = 2kn_a c \quad (3.6)$$

$$\phi_s = 2k(n_s - n_a)\sqrt{c^2 - x'^2} \quad (3.7)$$

$$\phi_{cl} = 2k(n_{cl} - n_s)\sqrt{b^2 - x'^2} \quad (3.8)$$

$$\phi_{co} = 2k(n_{co} - n_{cl})\sqrt{a^2 - x'^2} \quad (3.9)$$

The field at x' plane $U'(x')$ for different regions becomes:

$$U'_1(P) = A(x)\exp(ikz)\exp(-i\phi_a), \quad x' > c \quad (3.10)$$

$$U'_2(P) = A(x)\exp(ikz)\exp(-i[\phi_a + \phi_s]), \quad b < x' < c \quad (3.11)$$

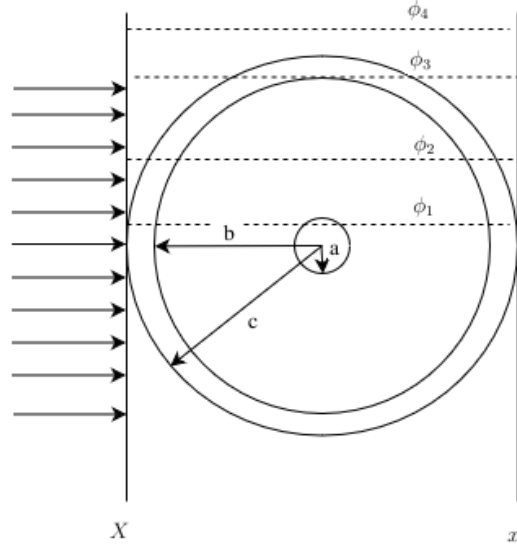


Figure 3.2. Optical path lengths for different regions

$$U'_3(P) = A(x)\exp(ikz)\exp(-i[\phi_a + \phi_s + \phi_{cl}]), \quad a < x' < b \quad (3.12)$$

$$U'_4(P) = A(x)\exp(ikz)\exp(-i[\phi_a + \phi_s + \phi_{cl} + \phi_{co}]), \quad -a < x' < a \quad (3.13)$$

$$U'_5(P) = A(x)\exp(ikz)\exp(-i[\phi_a + \phi_s + \phi_{cl}]), \quad -b < x' < -a \quad (3.14)$$

$$U'_6(P) = A(x)\exp(ikz)\exp(-i[\phi_a + \phi_s]), \quad -c < x' < -b \quad (3.15)$$

$$U'_7(P) = A(x)\exp(ikz)\exp(-i\phi_a), \quad x' < -c \quad (3.16)$$

The field at a point (P) on the observation plane can be found by near field Huygens-Fresnel diffraction integral:

$$U''(P) = -\frac{1}{4\pi} \sum_{x=-\infty}^{\infty} \left(ik(1 + \cos\theta) - \frac{\cos\theta}{r} \right) \frac{\exp(ikr)}{r} U'(x') \quad (3.17)$$

where the obliquity factor $\cos\theta = \frac{x-x'}{z}$ and the intensity obtained on the screen for three layer phase object is

$$I = (U''(P))(U''(P))^* \quad (3.18)$$

where * represents the complex conjugate.

3.1.1.2. Exact Ray Tracing

The same procedure is followed as we have done in previous part except that the rays are traced exactly in phase and amplitude. The exact points on x' plane where the rays propagate after multi-refractions are found and near field Huygens-Fresnel diffraction integral evaluated. Since the refractive index difference between core and cladding $\Delta n \ll 1$, $n_{co} \approx c_{cl}$ is taken and the calculations are made in two layer geometry.

The applied field at X plane can be defined as

$$U(x, 0, z) = A(x) \exp(ikz) \quad (3.19)$$

In the Figure 3.3, b is the radius cladding and the c is the radius of coating. The optical path for a ray Δd is

$$\Delta d = n_a(\overline{AB} + \overline{EF}) + n_s(\overline{BC} + \overline{DE}) + n_{cl}\overline{CD} \quad (3.20)$$

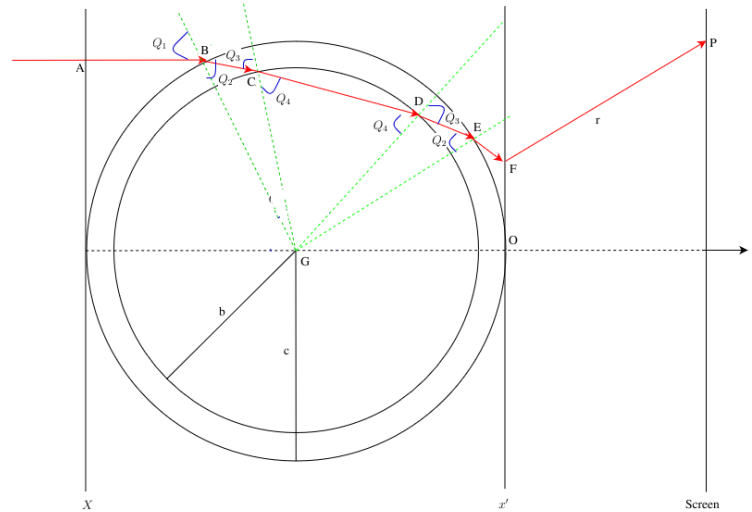


Figure 3.3. The optical path for a ray

The Snell's law is used in every refraction. In the first refraction at point B

$$n_a \sin \theta_1 = n_s \sin \theta_2 \quad (3.21)$$

$$\theta_2 = \sin^{-1}\left(\frac{n_a \sin \theta_1}{n_s}\right) \quad (3.22)$$

$$\overline{AB} = c - c \cos \theta_1 \quad (3.23)$$

using cosine theorem to find \overline{BC}

$$b^2 = \overline{BC}^2 - 2c\overline{BC} \cos \theta_2 + c^2 \quad (3.24)$$

$$\overline{BC} = c \cos \theta_2 - \sqrt{c^2 \cos^2 \alpha_1 - (c^2 - b^2)} \quad (3.25)$$

the incidence angle at point C

$$\theta_3 = 180^\circ - \cos^{-1}\left(\frac{b^2 + \overline{BC}^2 - c^2}{2b\overline{BC}}\right) \quad (3.26)$$

using Snell's law to find refraction angle

$$n_s \sin \theta_3 = n_{cl} \sin \theta_4 \quad (3.27)$$

$$\theta_4 = \sin^{-1}\left(\frac{n_s \sin \theta_3}{n_{cl}}\right) \quad (3.28)$$

$$\overline{CD} = 2b \cos \theta_4 \quad (3.29)$$

the Snell's law at point D

$$n_{cl} \sin \theta_4 = n_s \sin \theta_3 \quad (3.30)$$

$$\theta_3 = \sin^{-1}\left(\frac{n_{cl} \sin \theta_4}{n_s}\right) \quad (3.31)$$

Also G using similarity theorem on BGC and EGD triangles to find \overline{DE}

$$\overline{DE} = \overline{BC} \quad (3.32)$$

the Snell's law at point E

$$n_s \sin \theta_2 = n_a \sin \theta_1 \quad (3.33)$$

$$\theta_1 = \sin^{-1}\left(\frac{n_s \sin \theta_2}{n_a}\right) \quad (3.34)$$

$$\overline{EQ} \approx \overline{AB} \quad (3.35)$$

the last path length \overline{EF} can be expressed as

$$\overline{EF} = c \frac{\cos(2(\theta_4 - \theta_3 + \theta_2) - \theta_1) - 1}{\cos(2(\theta_4 - \theta_3 + \theta_2 - \theta_1))} \quad (3.36)$$

to express $x' = \overline{OF}$

$$x' = c \sin \theta_1 \left(1 + \tan(2(\theta_1 - \theta_2)) - \frac{\sin \theta_1}{\cos(2(\theta_1 - \theta_2))}\right) \quad (3.37)$$

to obtain the exact amplitude at x' for each ray

$$A(x') = t_1 t_2 t_3 t_4 A(x) \quad (3.38)$$

where t_1 t_2 t_3 and t_4 are amplitude transmission coefficients and is $A(x)$ the amplitude at point B.

The field at x' plane $U'(x')$ for different regions becomes:

$$U'(x') = A(x') \exp(ikz) \exp(-ik\Delta d) \quad (3.39)$$

The field at a point (P) on the observation plane can be found by near field Huygens-Fresnel diffraction integral:

$$U''(P) = -\frac{1}{4\pi} \sum_{x=-\infty}^{\infty} \left(ik(1 + \cos\theta) - \frac{\cos\theta}{r} \right) \frac{\exp(ikr)}{r} U'(x') \quad (3.40)$$

where the obliquity factor $\cos\theta = \frac{x-x'}{r}$. The intensity obtained on the screen for three layer phase object is

$$I = (U''(P))(U''(P))^* \quad (3.41)$$

where * represents the complex conjugate.

In paraxial approach, the deflections of the rays are omitted. However, it can be deduced that paraxial ray tracing gives us nearly same diffraction pattern with exact ray tracing. The comparison of two methods is given in figure 3.4.

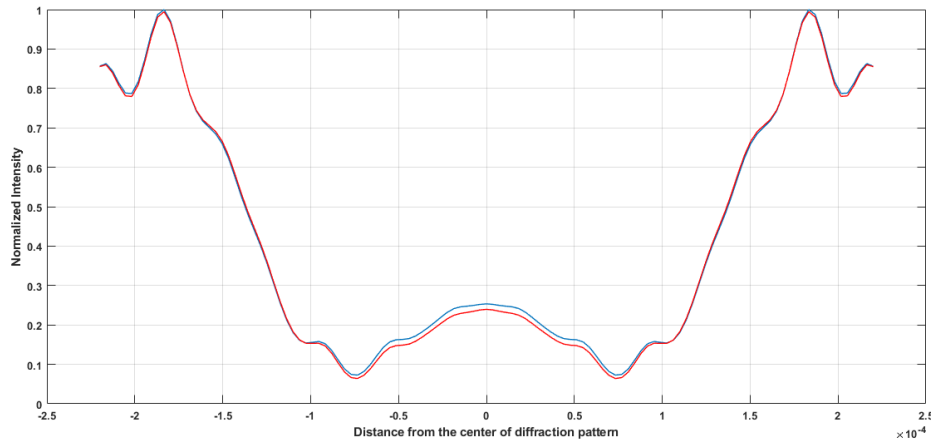


Figure 3.4. Simulations of the normalized intensity distributions 100 nm coated optical fiber diffraction pattern in air where the distance is 5cm with the observation plane, exact tracing(red) and paraxial tracing(blue)

3.1.2. Structured Light Modes

In this part, the cylindrical phase object is examined with paraxial approximation and guided modes. The source is obtained by using step-index optical fiber. The far-field radiation mode from the fiber end obtained by Fraunhofer approximation. After the wavefront obtained at the beginning of the coated optical fiber, the same paraxial ray tracing procedure in the previous part is used.

The propagating field mode in optical fiber defined in mathematical preliminaries section as:

$$\psi_i(\rho, \phi_0) = AJ_v(\kappa\rho)\cos(v\phi_0) \quad \rho < a \quad (3.42)$$

$$\psi_i(\rho, \phi_0) = A\frac{J_v(U)}{K_v(W)}K_v(i\gamma\rho)(\kappa\rho)\cos(v\phi_0) \quad \rho > a \quad (3.43)$$

where $U = \kappa a$, $W = \gamma a$ and a is the radius of optical fiber core and

$$b = 1 - \frac{U^2}{W^2} = \frac{(\beta^2/k^2) - n_{cl}^2}{n_{co}^2 - n_{cl}^2} \quad (3.44)$$

where β is the propagation constant, k is the wavenumber in free space, n_{co} is the refractive index of core and n_{cl} is the refractive index of cladding. Also

$$\kappa = \sqrt{n_{co}^2 k^2 - \beta^2} \quad (3.45)$$

$$\gamma = \sqrt{\beta^2 - n_{cl}^2 k^2} \quad (3.46)$$

The far field radiation can be defined as (Boncek and Rode, 1991)

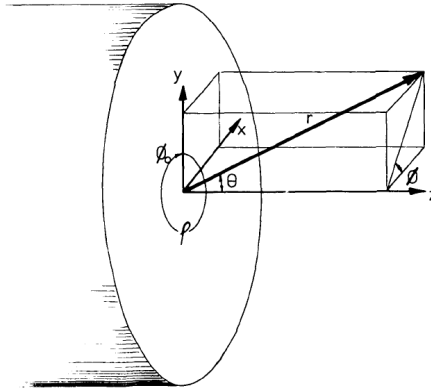


Figure 3.5. Optical fiber geometry for far field calculations (Gambling et al., 1976)

$$\psi(\rho, \theta, \phi) = \frac{i \exp(-ikr)}{\lambda r} \left\{ \int_0^{2\pi} \int_0^a J_v(\kappa\rho)\cos(v\phi_0) \exp(ik\rho \sin \theta \cos(\phi - \phi_0)) \rho d\rho d\phi \right. \\ \left. + \int_0^{2\pi} \int_a^\infty \frac{J_v(U)}{K_v(W)} K_v(i\gamma\rho)(\kappa\rho)\cos(v\phi_0) \exp(ik\rho \sin \theta \cos(\phi - \phi_0)) \rho d\rho d\phi \right\} \quad (3.47)$$

where $\nu = 0$ and $\nu = 1$ represents LP01 and LP11 modes respectively.

The obtained field can be defined as a source for the cylindrical phase object. The field at X plane is $\psi(x)$ in Figure 3.6.

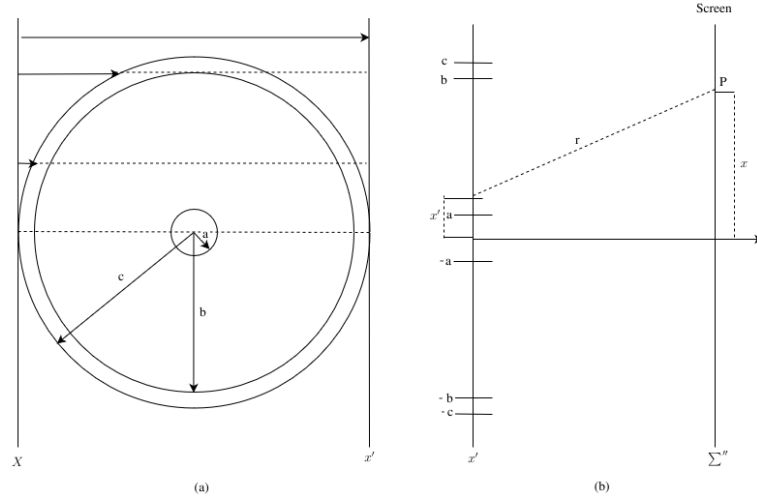


Figure 3.6. (a) Linearly polarized field passing through cylindrical object, (b) Diffraction from cylindrical object

The phase variations for different rays were defined in paraxial ray tracing part from Equation (3.6) to (3.9). Using these phase variations, the field at x' plane can be defined as

$$U'_1(P) = \psi(x) \exp(ikz) \exp(-i\phi_a), \quad x' > c \quad (3.48)$$

$$U'_2(P) = \psi(x) \exp(ikz) \exp(-i[\phi_a + \phi_s]), \quad b < x' < c \quad (3.49)$$

$$U'_3(P) = \psi(x) \exp(ikz) \exp(-i[\phi_a + \phi_s + \phi_{cl}]), \quad a < x' < b \quad (3.50)$$

$$U'_4(P) = \psi(x) \exp(ikz) \exp(-i[\phi_a + \phi_s + \phi_{cl} + \phi_{co}]), \quad -a < x' < a \quad (3.51)$$

$$U'_5(P) = \psi(x) \exp(ikz) \exp(-i[\phi_a + \phi_s + \phi_{cl}]), \quad -b < x' < -a \quad (3.52)$$

$$U'_6(P) = \psi(x) \exp(ikz) \exp(-i[\phi_a + \phi_s]), \quad -c < x' < -b \quad (3.53)$$

$$U'_7(P) = \psi(x) \exp(ikz) \exp(-i\phi_a), \quad x' < -c \quad (3.54)$$

The field at a point (P) on the observation plane can be found by near field Huygens-Fresnel diffraction integral:

$$U''(P) = -\frac{1}{4\pi} \sum_{x=-\infty}^{\infty} \left(ik(1 + \cos\theta) - \frac{\cos\theta}{r} \right) \frac{\exp(ikr)}{r} U'(x') \quad (3.55)$$

The intensity obtained on the screen for three layer phase object is

$$I = (U''(P))(U''(P))^* \quad (3.56)$$

CHAPTER 4

EXPERIMENTAL SETUP, MEASUREMENTS AND RESULTS

4.1. Experimental Setup

In this chapter, measurement of nanoscale dielectric films on curved surfaces is shown experimentally by using near field Huygens Fresnel diffraction method. The measurements contain three different light sources which are plane wave and optical fiber modes. The experimental procedure can be divided into two parts: coating of fiber optic and measurements.

In coating of fiber optic process, Layer by Layer assembly technology (Richardson et al., 2015) was chosen because of the fact that there is needed to obtain nanoscale coatings and this technology shows that film thickness can be obtained up to 3 nanometer. The LBL technology divided into 5 major techniques: dip (immersive) coating, spin coating, spray coating, electromagnetic coating and fluid coating. At this point, dip coating was decided to use because of easy implementation.

After choosing of coating technique next decision is about the coating materials. We need transparent materials at the wavelength of interest. The combination of Poly acrylic acid (PAA) and Polyethylenimine (PEI) is useful to obtain transparent coating. PEI represents the cationic polymer whereas PAA anionic polymer.

The coating process starts with the cleaning of optical fiber with Isopropyl Alcohol. Then, optical fiber was first dipped into cationic solution (PEI) for 5 min, followed by rinsing distilled water for 30 s and drying. This process creates the first positively charged layer of fiber. The same cycle was applied to obtain first negatively charged layer by using PAA. The obtaining of first bilayer which is created by positively and negatively charged layers is called one deposition. Starting from the second deposition cycle, the dipping times reduced to 3 min. This process is repeated to obtain desired film thickness.

The film thickness is shown an alteration according to pH (Yang et al., 2011), deposition time (Zang et al., 2012) and drying (Yang et al., 2010). The pH of PAA and PEI was chosen to obtain thicker films. Besides, the drying cycle was used to reduce

roughness of surface of film. The deposition process of dip coating LBL is given in Figure 4.1.

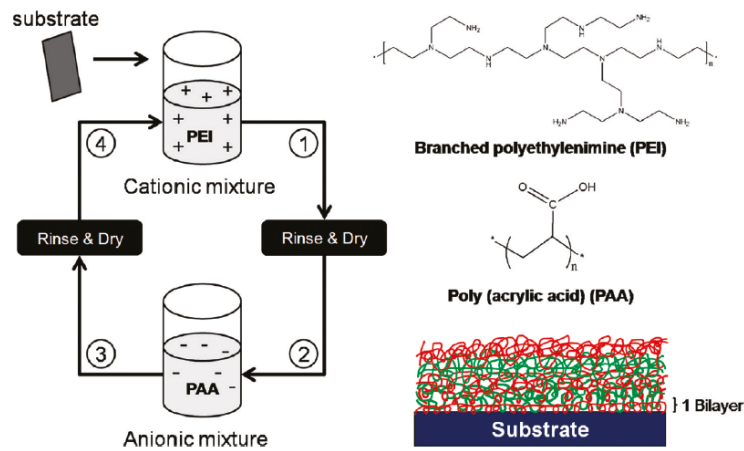


Figure 4.1. Schematic of the layer-by-layer deposition process (Yang et al., 2011)

The next part is the measurement of coating thickness after LBL assembly. A schematic of the measurement setup are sketched for plane wave and LP modes in Figure 4.2 and 4.4 respectively. Therefore, we examine the experimental setup into two category.

- Plane wave:** The setup starts with the generation and sending of plane wave to the polymer coated optical fiber. Then, the sensor array (Sony *IMX219*) record the diffraction pattern. The sensor array has $1.12\mu m \times 1.12\mu m$ pixel size. The small differences in diffraction pattern can be observed by the contribution of small pixel size. The distance between the sensor array and coated optical fiber is approximately $600\mu m$. At the end normalized intensity of diffraction pattern and mathematical model are fitted.

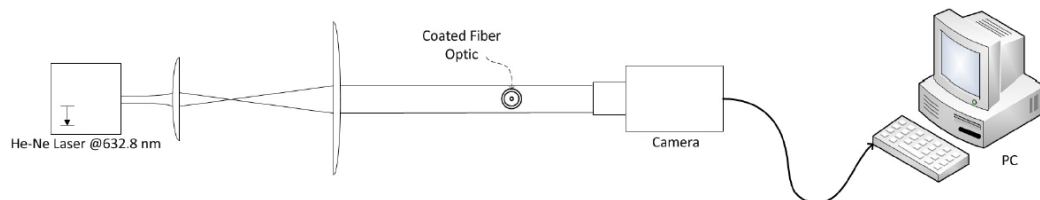


Figure 4.2. Experimental setup for estimation of thickness by using plane wave

- LP Modes:** The setup starts with the conversion of the output of 632.8 nm He-Ne laser light beam to LP modes by using step index optical fiber. The obtained LP modes are LP_{01} and LP_{11} . The distances from first fiber end to coated fiber are 4 mm and 1.3 mm for LP_{01} and LP_{11} respectively. The expected fields which reach the coated optical fiber are given in Figure 4.3. The diffraction patterns are recorded by sensor array. The distances between the sensor array and coated optical fiber are approximately $600 \mu\text{m}$ and $200 \mu\text{m}$ for LP_{01} and LP_{11} , respectively. At the end normalized intensity of diffraction pattern and mathematical model are fitted.

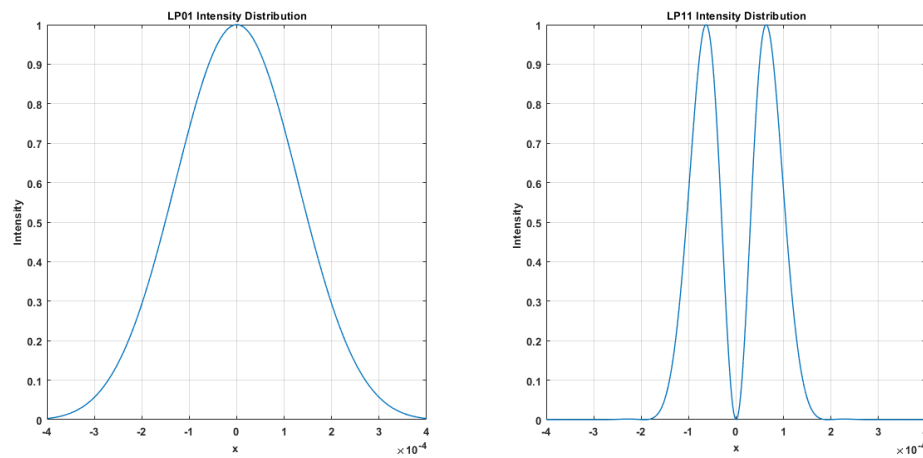


Figure 4.3. Intensity distributions of LP_{01} and LP_{11} at the beginning of coated fiber

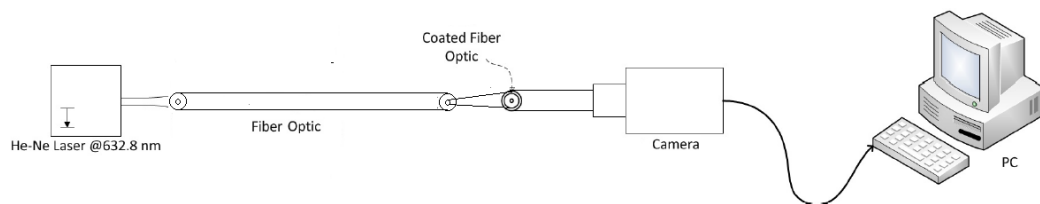


Figure 4.4. Experimental setup for estimation of thickness by using structured light

The intensity and diffraction pattern profiles are given in Figure 4.5. It can be easily concluded that diffraction patterns shows differences according to the applied sources.

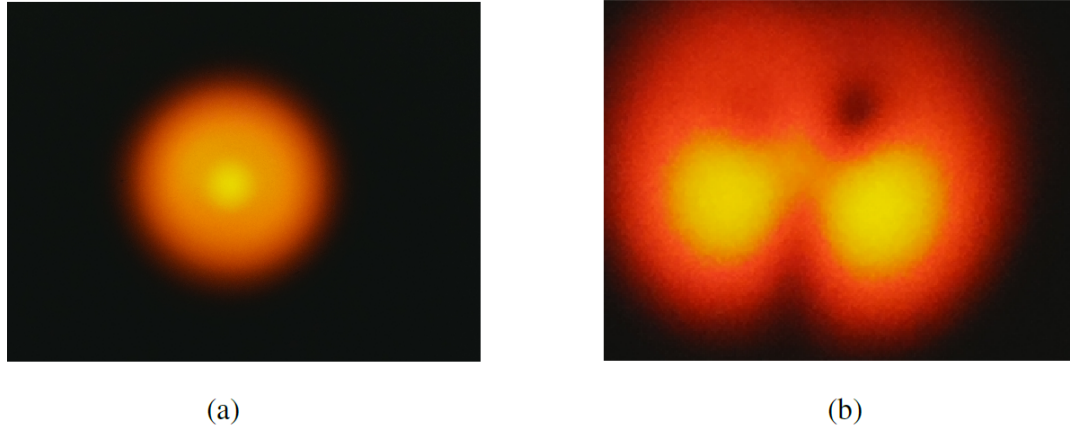


Figure 4.5. Applied source intensity patterns: (a) LP01 mode (b) LP11 mode

4.2. Measurement Results

This section includes three subsection according to the selection of source types. Besides, the measurements were done for different coating thicknesses. There are many techniques for the characterization in the literature such as ellipsometry, profilometry, SEM etc. which were mentioned in Chapter 1. The most powerful is SEM since the others are not suitable for curved surface. Therefore, the results were compared with the Scanning Electron Microscope (SEM) results in order to verify our characterization technique.

The critical point is that SEM is very expensive device and it uses destructive method so optical fiber which is analysed can not be used again. Besides, dielectric materials raise difficulties to it. Therefore, there is needed some preparation before the measurements such as coating with gold plate to the optical fiber. To overcome these negative aspects of SEM and other techniques, we propose simple, non-destructive, real time and cheap method for the optical characterization of curved surfaces.

Determination of distance between optical fiber and sensor array is important since optical fiber behaves as a ball lens. The light is focused by the core and cladding of fiber at different points. The focal points of core and cladding can be seen in Figure 4.6 where $f_1 \approx 38\mu m$ and $f_2 \approx 534\mu m$. If the sensor array is placed near the focal point of cladding, deviations on diffraction pattern can not be observable. The phase contributions of rays which have long optical path length in transparent film makes the difference. In

this way, the thickness variation becomes measurable for sub-wavelength thicknesses. However, if all rays focus to narrower region around the focal point, phase contributions of film are lost. Therefore, the effective distance between optical fiber and sensor array has to be determined before the measurements.

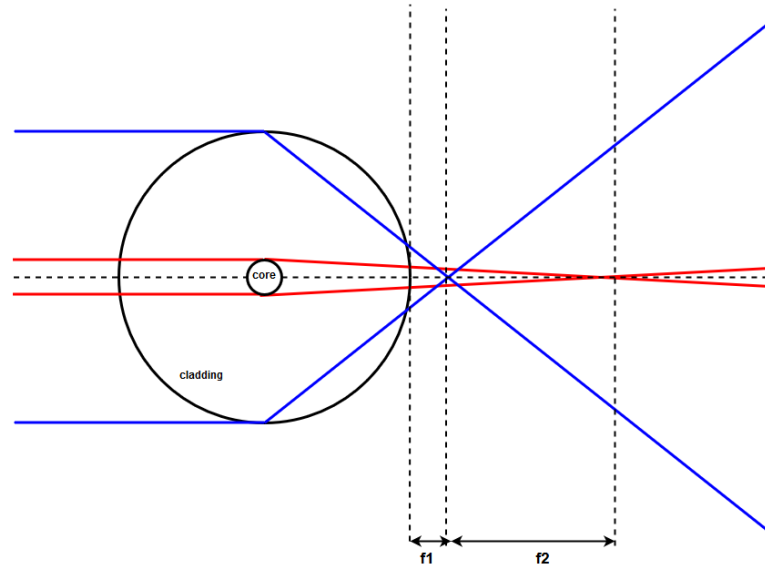


Figure 4.6. Focal points of core and cladding

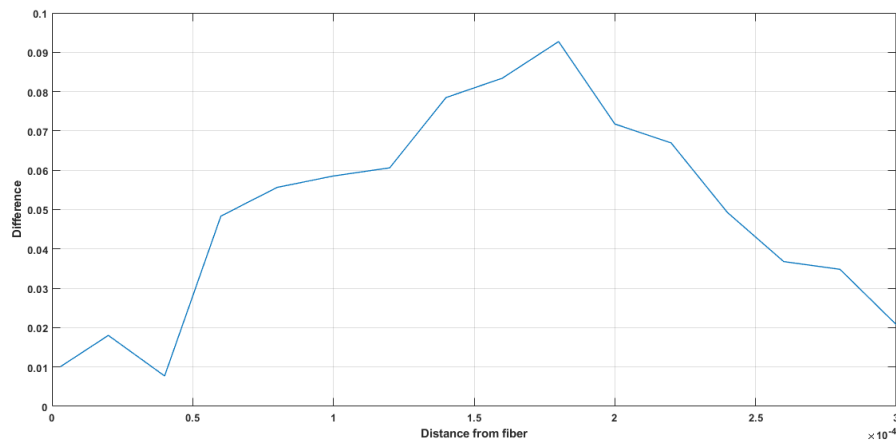


Figure 4.7. Deviation between non-coated and 70 nm coated fiber for different distances between optical fiber and sensor array (LP11 illumination)

4.2.1. Plane Wave Results

- Non-coated optical fiber measurements where the distances between optical fiber and sensor array is $600\ \mu\text{m}$. The mathematical model and experimental result fitting is given in Figure 4.8. The diffraction pattern on sensor array and SEM results are given below.

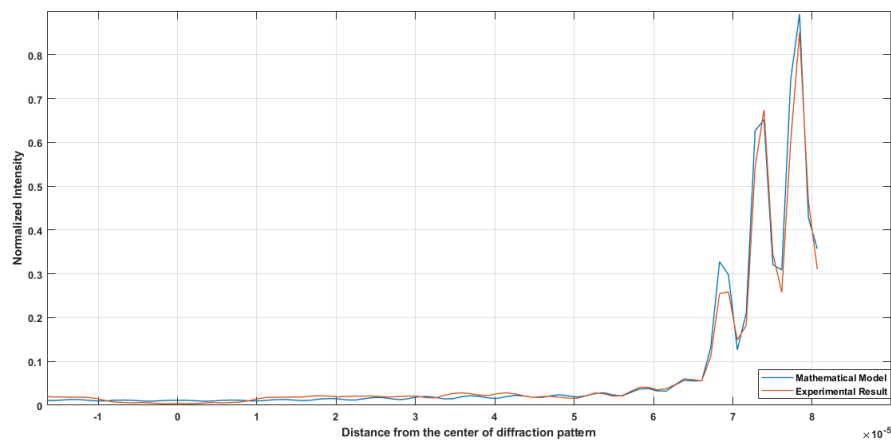


Figure 4.8. Non-coated optical fiber-1: The experimental intensity fitted at non-coating of optical fiber

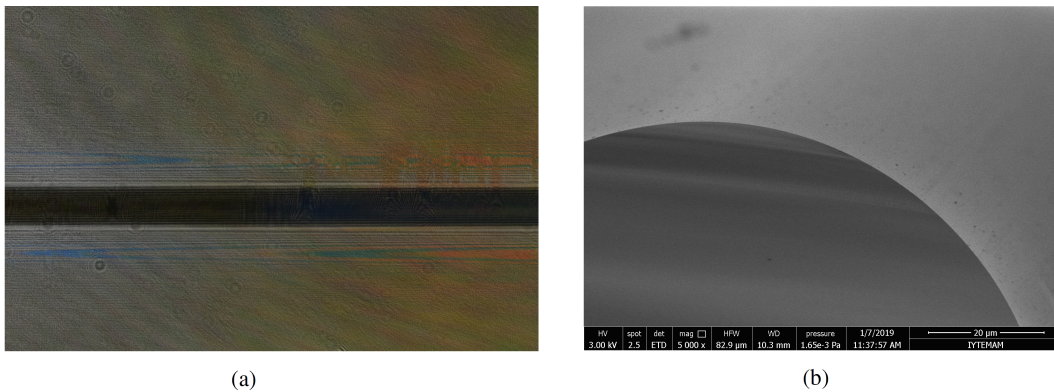


Figure 4.9. (a) Diffraction pattern recorded by sensor array (b) SEM result of non-coated optical fiber

- 183.5 nm coated optical fiber measurements where the distances between optical fiber and sensor array is 600 μm . The mathematical model and experimental result fitting is given in Figure 4.10. The diffraction pattern on sensor array and SEM results are given below.

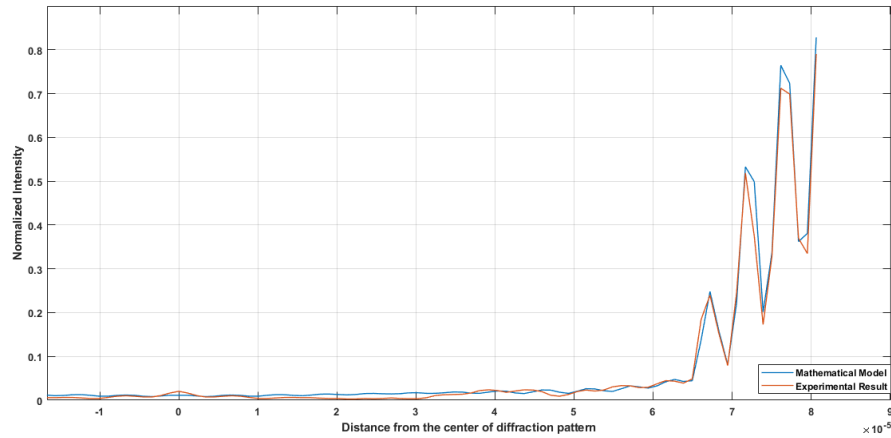


Figure 4.10. Polymer coated optical fiber-2: The experimental intensity fitted at 180 nm coated optical fiber

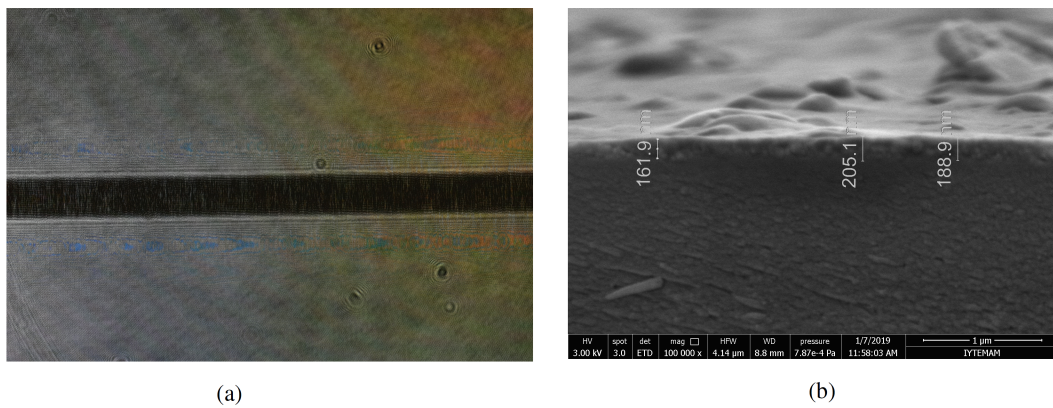


Figure 4.11. (a) Diffraction pattern recorded by sensor array (b) SEM result of coated optical fiber about 183.5 nm

- 67 nm coated optical fiber measurements where the distances between optical fiber and sensor array is 600 μm . The mathematical model and experimental result fitting is given in Figure 4.12. The diffraction pattern on sensor array and SEM results are given below.

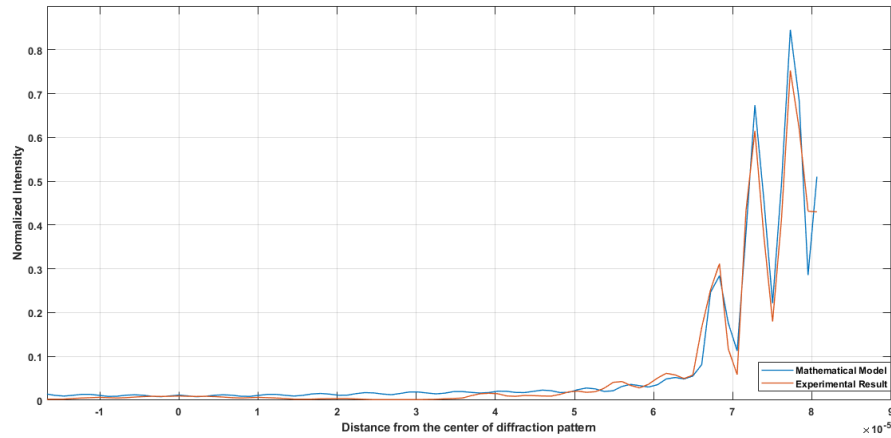


Figure 4.12. Polymer coated optical fiber-3: The experimental intensity fitted at 79 nm coated optical fiber

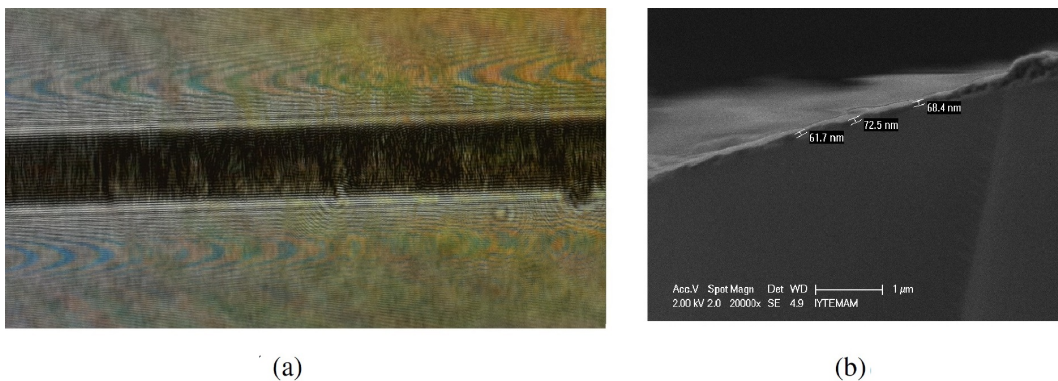


Figure 4.13. (a) Diffraction pattern recorded by sensor array (b) SEM result of coated optical fiber about 67 nm

- The experimental data comparisons are given in Figure 4.14 and 4.15. The diffraction pattern shows observable differences in thicker coatings. When the thickness is getting smaller, the prediction is getting worse and become unstable for different recorded photos since the difference between non-coated and coated fibers becomes unobservable.

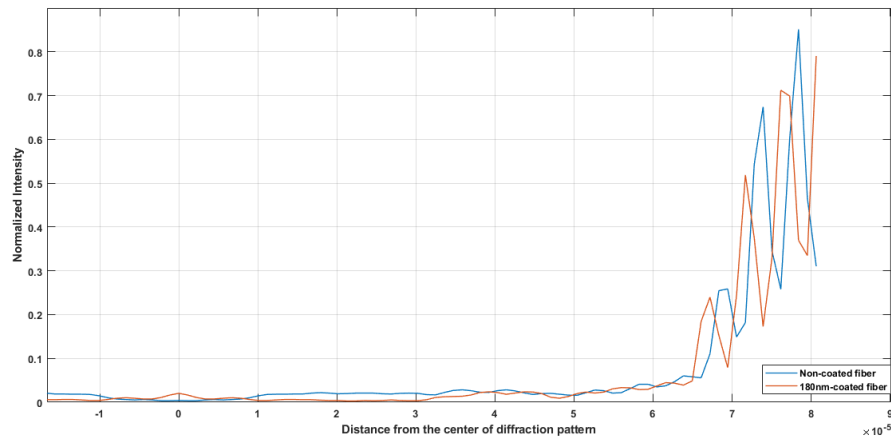


Figure 4.14. Plane wave experimental results of non-coated and 180 nm coated optical fibers

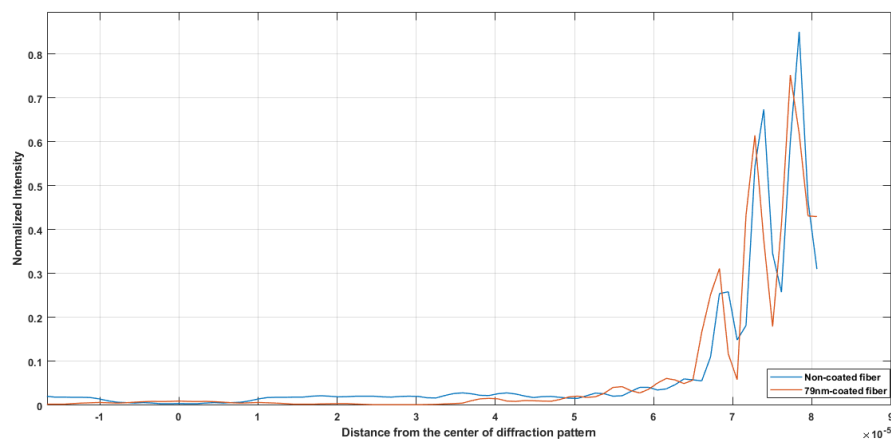


Figure 4.15. Plane wave experimental results of non-coated and 79 nm coated optical fibers

4.2.2. LP01 Mode Results

- Non-coated optical fiber measurements where the distances between optical fiber and sensor array is $600 \mu m$. Also, the distance between source optical fiber end and coated optical fiber is $4 mm$. The mathematical model and experimental result fitting is given in Figure 4.16. The diffraction pattern on sensor array and SEM results are given below.

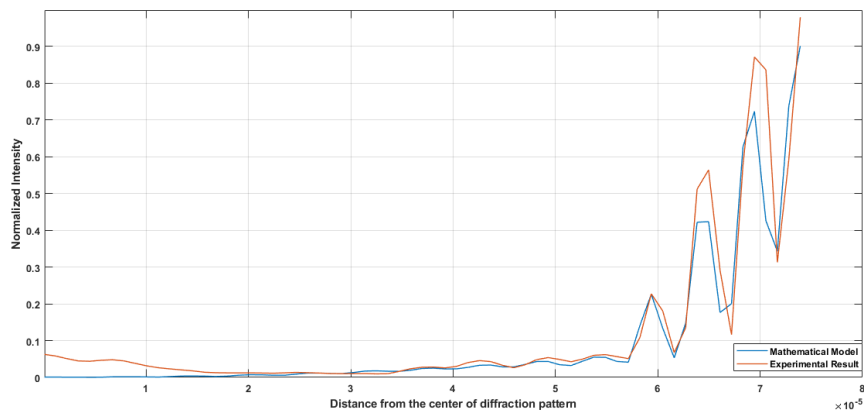


Figure 4.16. Non-coated optical fiber-1: The experimental intensity fitted at non-coating of optical fiber

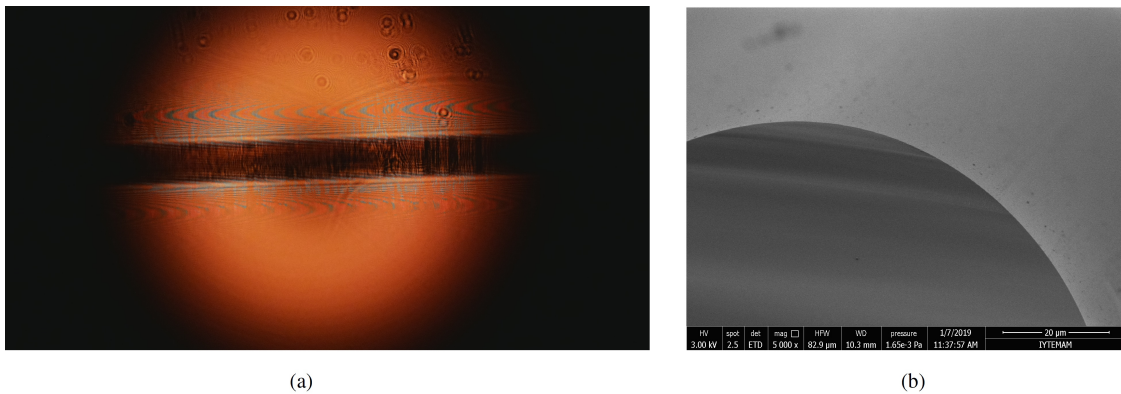


Figure 4.17. (a) Diffraction pattern recorded by sensor array (b) SEM result of non-coated optical fiber

- 183.5 nm coated optical fiber measurements where the distances between optical fiber and sensor array is 600 μm . Also, the distance between source optical fiber end and coated optical fiber is 4 mm. The mathematical model and experimental result fitting is given in figure 4.18. The diffraction pattern on sensor array and SEM results are given below.

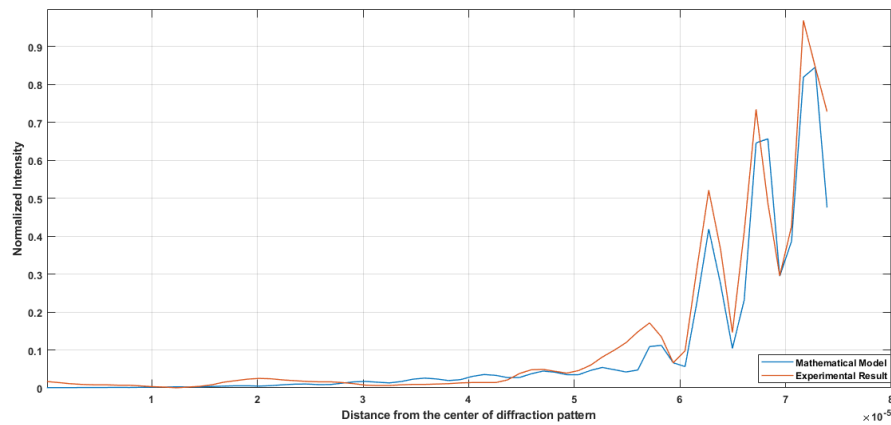


Figure 4.18. Polymer coated optical fiber-2: The experimental intensity fitted at 179 nm coated optical fiber

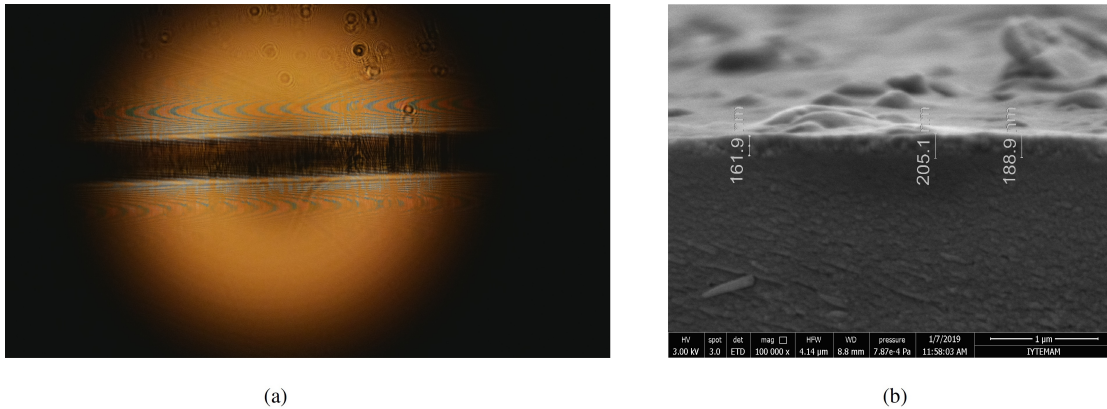


Figure 4.19. (a) Diffraction pattern recorded by sensor array (b) SEM result of coated optical fiber about 183.5 nm

- 67 nm coated optical fiber measurements where the distances between optical fiber and sensor array is 600 μm . Also, the distance between source optical fiber end and coated optical fiber is 4 mm The mathematical model and experimental result fitting is given in figure 4.20. The diffraction pattern on sensor array and SEM results are given below.

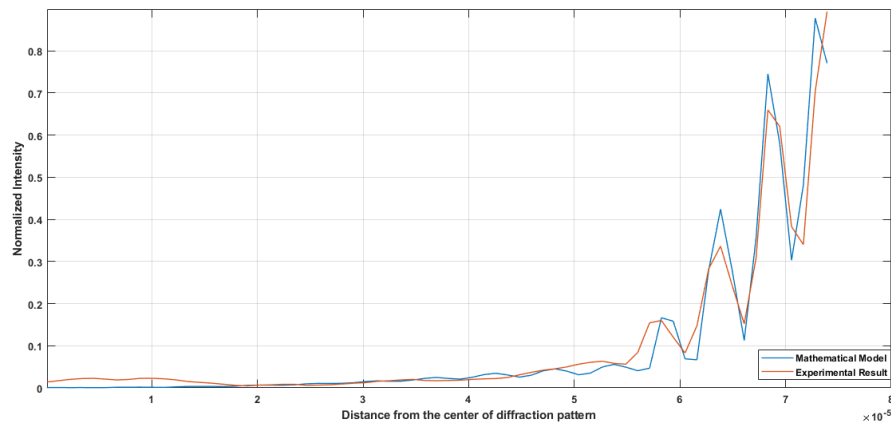


Figure 4.20. Polymer coated optical fiber-3: The experimental intensity fitted at 77 nm coated optical fiber

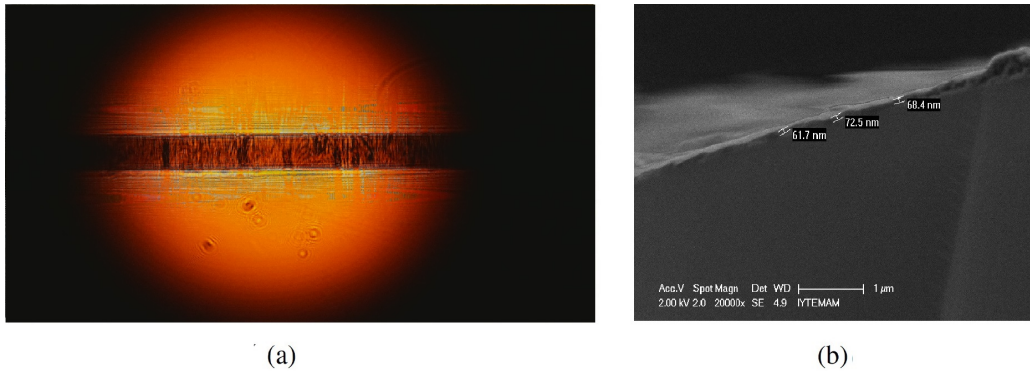


Figure 4.21. (a) Diffraction pattern recorded by sensor array (b) SEM result of coated optical fiber about 67 nm

- The experimental data comparisons are given in Figure 4.22 and 4.23. The diffraction pattern shows observable differences in thicker coatings. When the thickness is getting smaller, the prediction is getting worse and become unstable for different recorded photos since the difference between non-coated and coated fibers becomes unobservable.

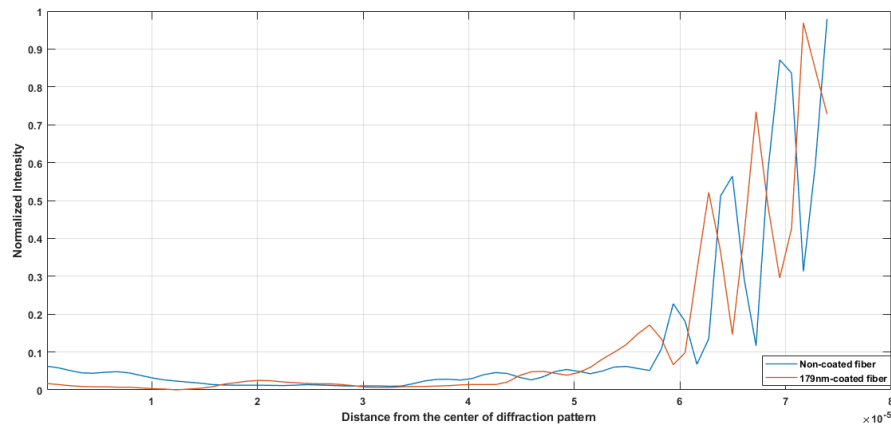


Figure 4.22. LP01 mode experimental results of non-coated and 179 nm coated optical fibers

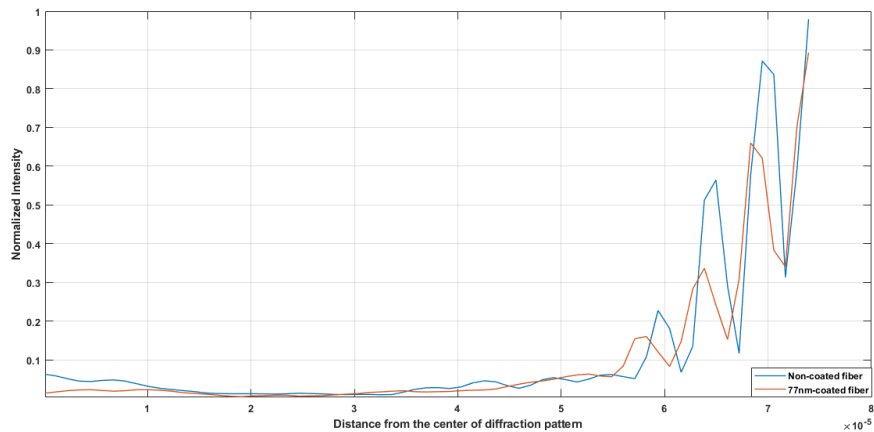


Figure 4.23. LP01 mode experimental results of non-coated and 77 nm coated optical fibers

4.2.3. LP11 Mode Results

- Non-coated optical fiber measurements where the distances between optical fiber and sensor array is approximately $200\ \mu\text{m}$. Also, the distance between source optical fiber end and coated optical fiber is approximately $1.3\ \text{mm}$. The mathematical model and experimental result fitting is given in Figure 4.24. The diffraction pattern on sensor array and SEM results are given below.

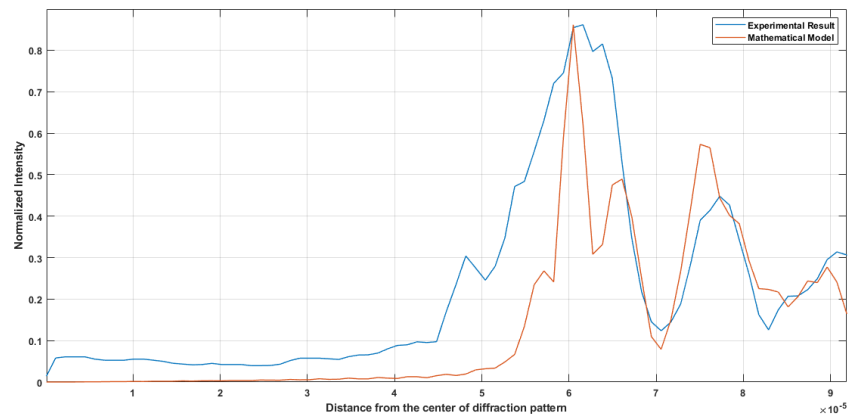


Figure 4.24. Non-coated optical fiber-1: The experimental intensity fitted at non-coating of optical fiber

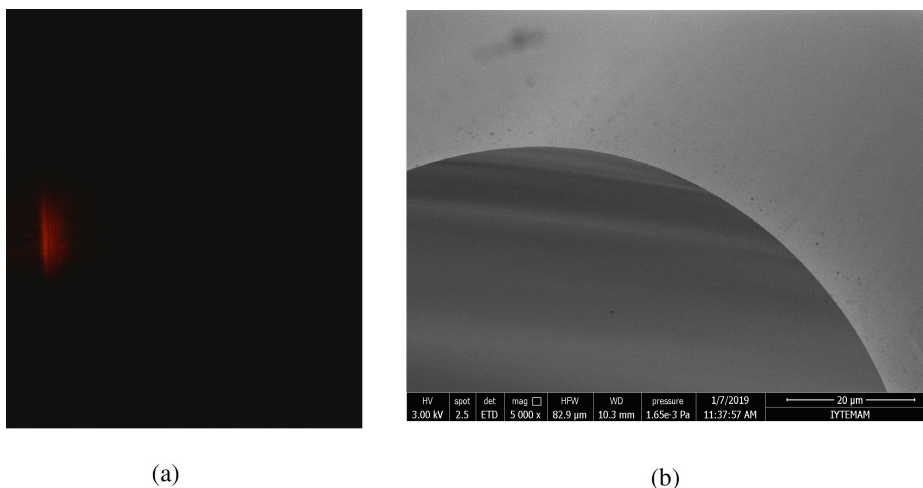


Figure 4.25. (a) Diffraction pattern recorded by sensor array (b) SEM result of non-coated optical fiber

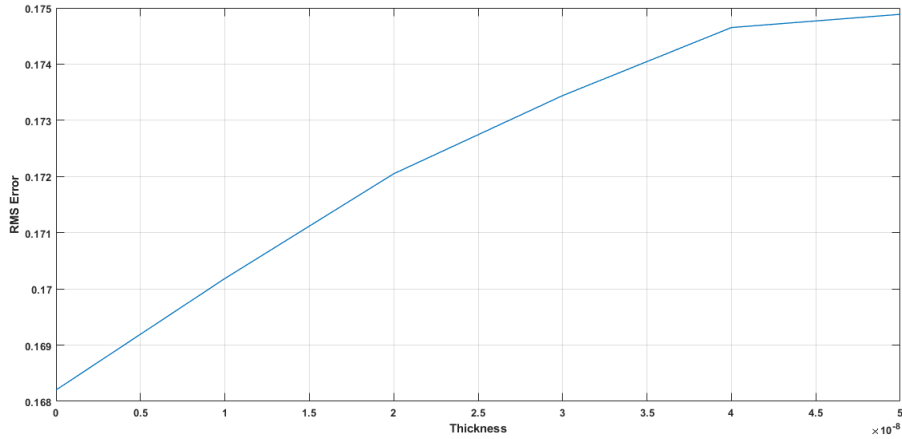


Figure 4.26. Error-Thickness variation for non-coated optical fiber

- 183.5 nm coated optical fiber measurements where the distances between optical fiber and sensor array is approximately 200 μm . Also, the distance between source optical fiber end and coated optical fiber is approximately 1.3 mm. The mathematical model and experimental result fitting is given in Figure 4.27. The diffraction pattern on sensor array and SEM results are given below.

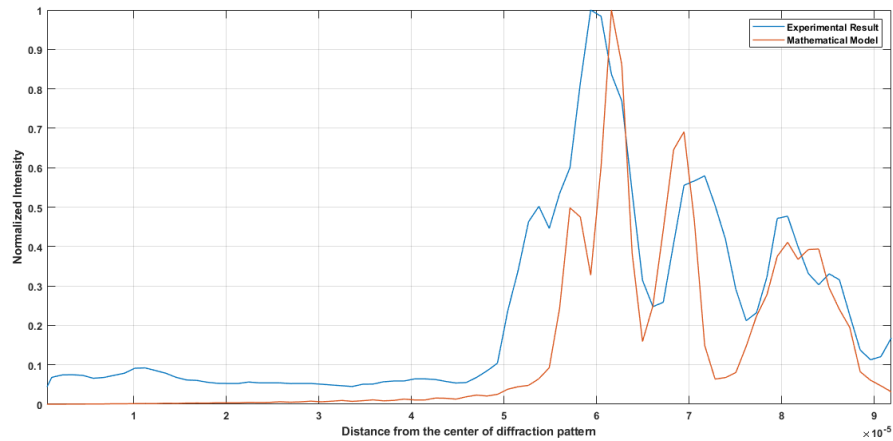


Figure 4.27. Polymer coated optical fiber-2: The experimental intensity fitted at 187 nm coated optical fiber

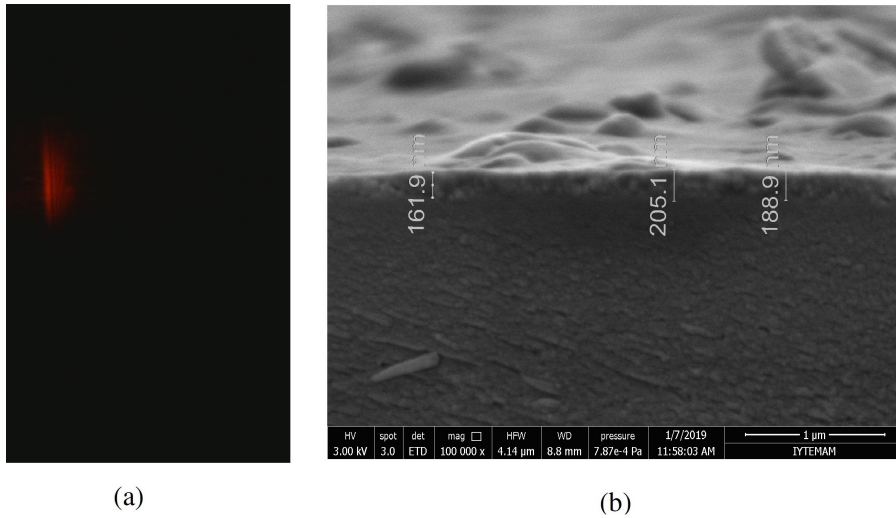


Figure 4.28. (a) Diffraction pattern recorded by sensor array (b) SEM result of coated optical fiber about 183.5 nm

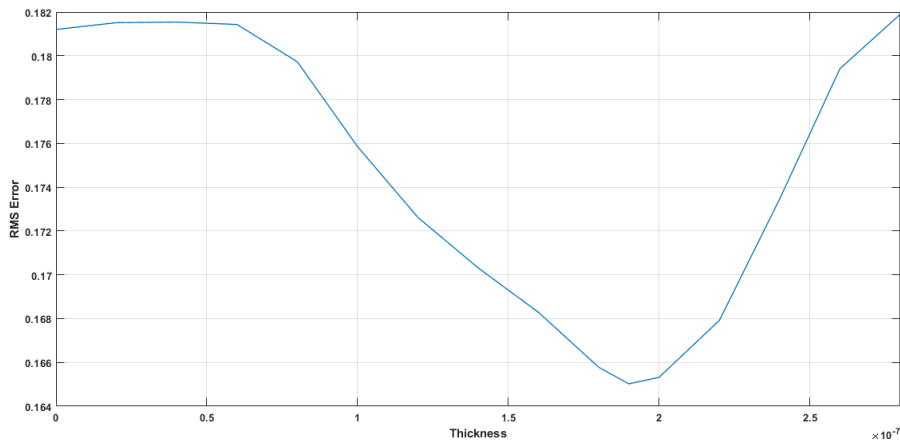


Figure 4.29. Error-Thickness variation for 187 nm coated optical fiber

- 67 nm coated optical fiber measurements where the distances between optical fiber and sensor array is approximately 200 μm . Also, the distance between source optical fiber end and coated optical fiber is approximately 1.3 mm. The mathematical model and experimental result fitting is given in Figure 4.30. The diffraction pattern on sensor array and SEM results are given below.

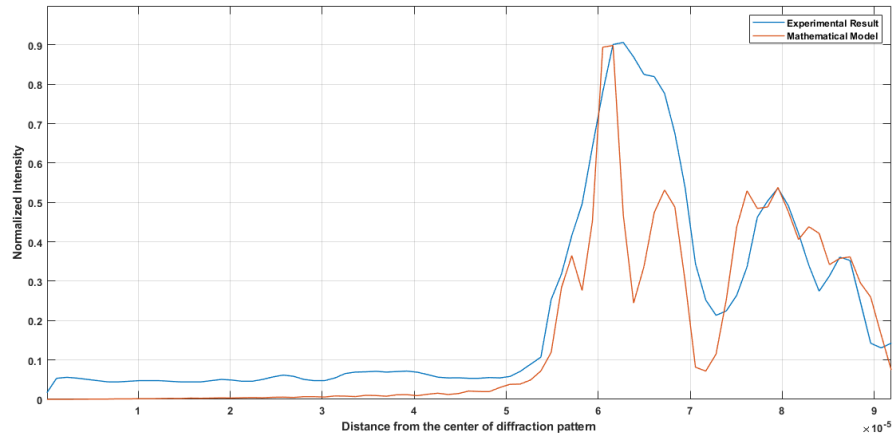


Figure 4.30. Polymer coated optical fiber-3: The experimental intensity fitted at 70 nm coated optical fiber

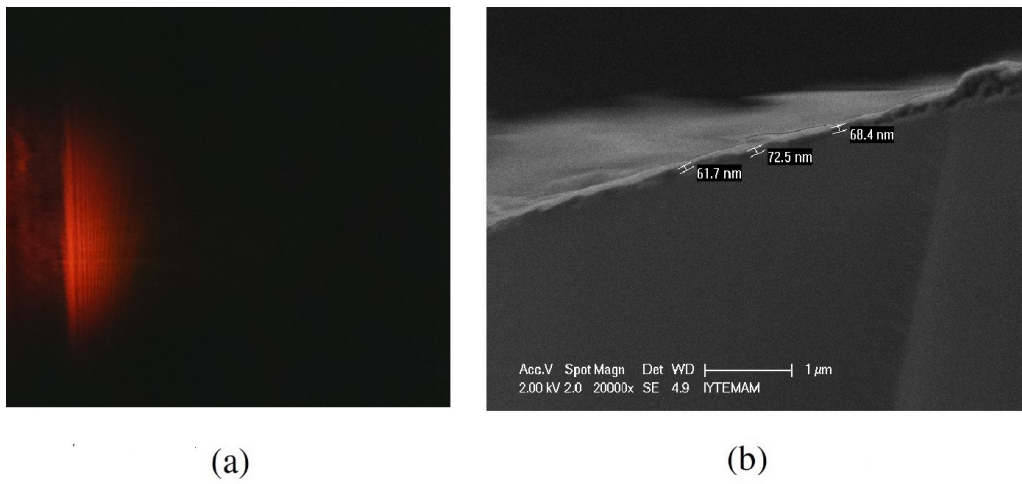


Figure 4.31. (a) Diffraction pattern recorded by sensor array (b) SEM result of coated optical fiber about 67 nm

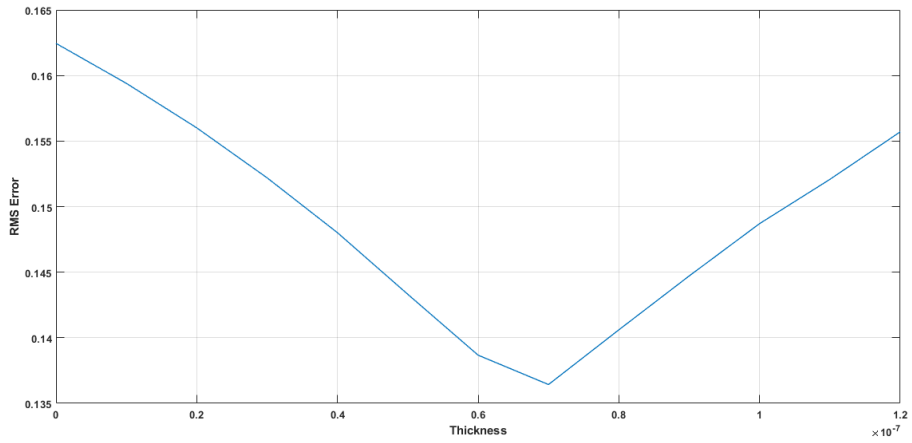


Figure 4.32. Error-Thickness variation for 70 nm coated optical fiber

- The theoretical and experimental data comparisons are given from Figure 4.33 to 4.37.

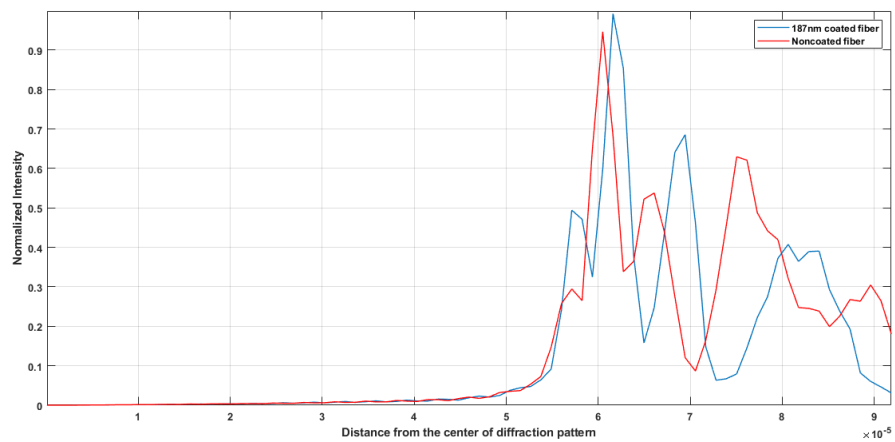


Figure 4.33. LP11 mode theoretical results of non-coated and 187 nm coated optical fibers

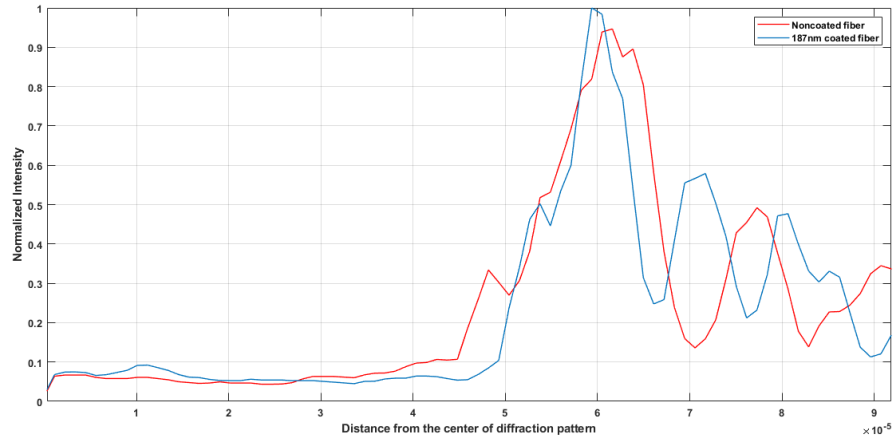


Figure 4.34. LP11 mode experimental results of non-coated and 187 nm coated optical fibers

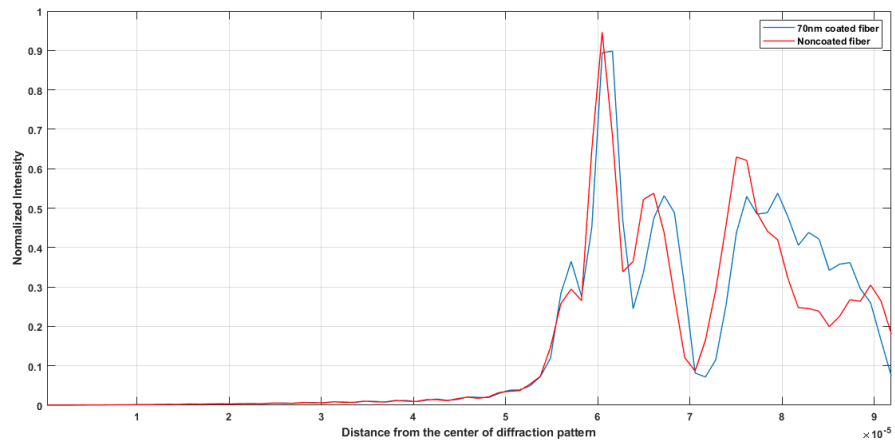


Figure 4.35. LP11 mode theoretical results of non-coated and 70 nm coated optical fibers

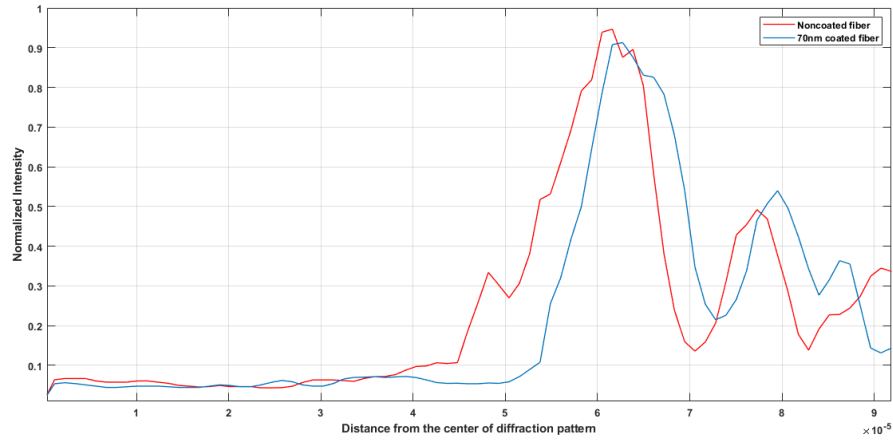


Figure 4.36. LP11 mode experimental results of non-coated and 70 nm coated optical fibers

4.2.4. Comparisons of Results

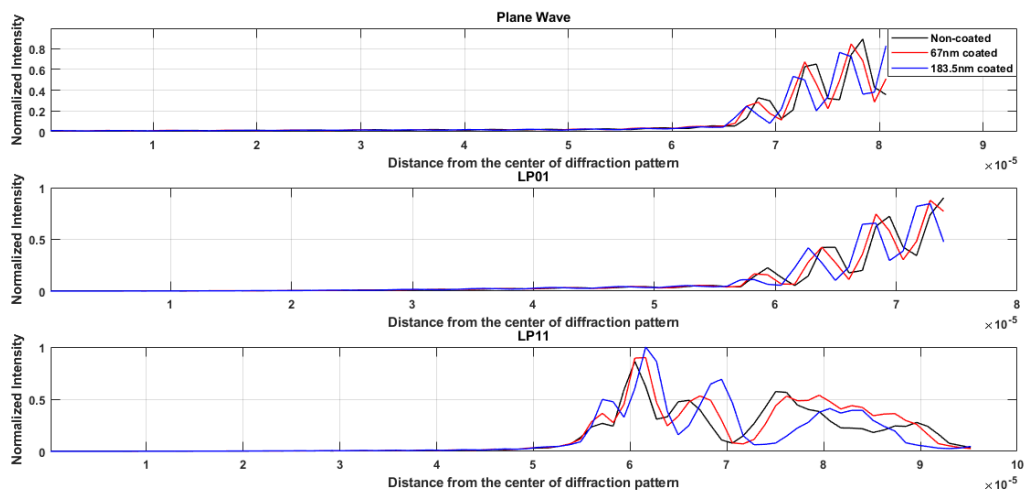


Figure 4.37. Simulation results of diffraction patterns for various sources

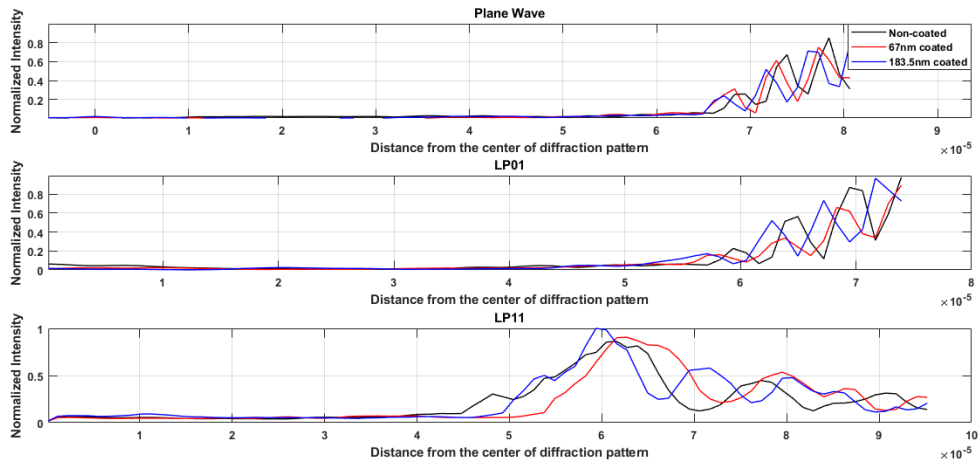


Figure 4.38. Experimental results of diffraction patterns for various sources

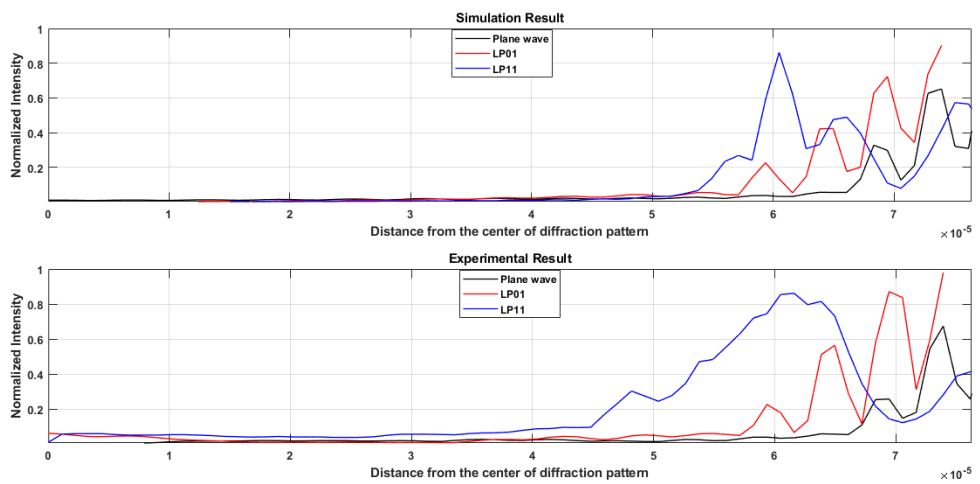


Figure 4.39. Non-coated optical fiber simulation and experimental results for plane wave, LP01 and LP11

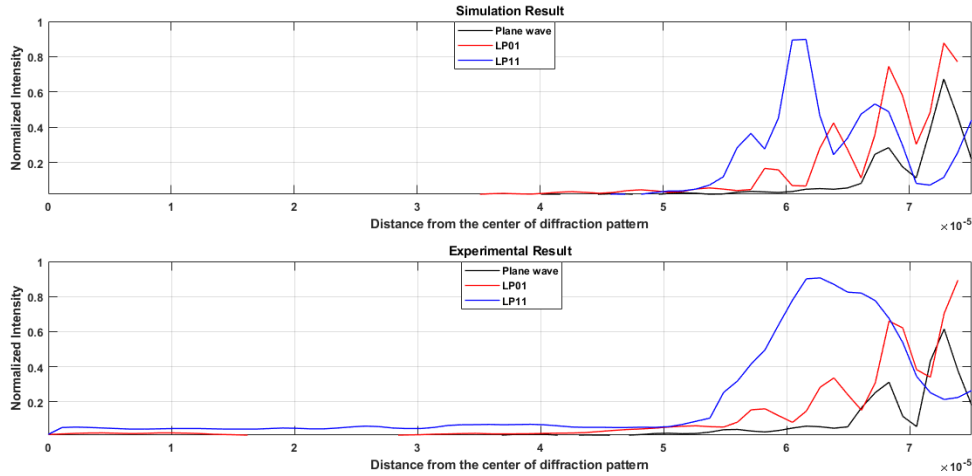


Figure 4.40. 67 nm coated optical fiber simulation and experimental results for plane wave, LP01 and LP11

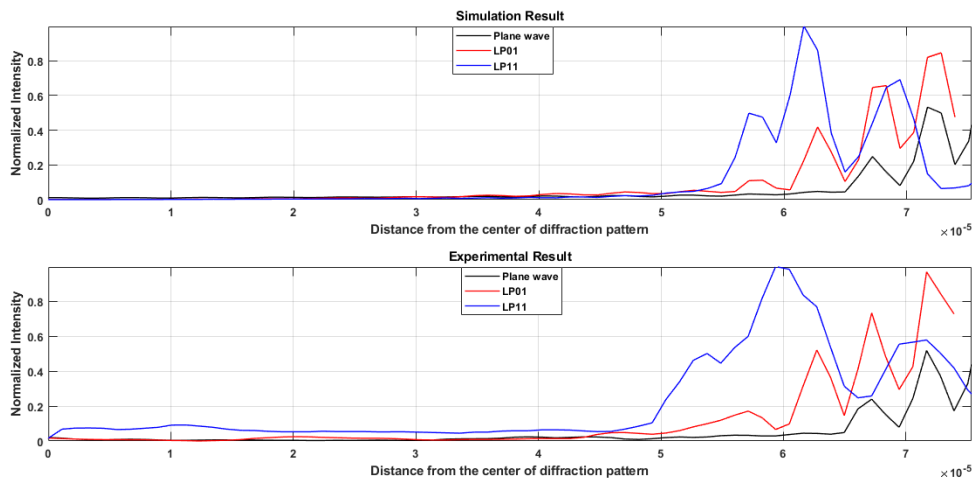


Figure 4.41. 183.5 nm coated optical fiber simulation and experimental results for plane wave, LP01 and LP11

4.3. Discussion

The results show that it is not possible to measure thickness below 50 nm. The reason is that not all near field terms are included in the diffraction formula. The distance between coated optical fiber and sensor array, represented by r in Equation 3.17, is 200 μm in the LP11 mode measurements and 600 μm in plane wave and LP01 mode

measurements. However, r must be smaller than 100 nm that evanescent terms become comparable with other terms or to dominate the formula.

$$k = \frac{2\pi}{\lambda} = \frac{2\pi}{632.8 \text{ nm}} = 6.929 \times 10^7 (1/m) \quad (4.1)$$

if $\cos \theta$ is taken 1

$$r \approx \frac{\cos \theta}{k} \approx 100 \text{ nm} \quad (4.2)$$

However, the minimum distance between coated optical and sensor array can be $3 \mu\text{m}$ according to the measurements. Therefore, the measurements can not be done at 100 nm .

The spatial frequency bandwidth can be calculated in order to observe the coating thickness below 50 nm . According to the uncertainty relation:

$$\Delta k \Delta r \geq 1 \quad (4.3)$$

Since Δr represents the thickness of film, the bandwidth of spatial frequencies Δk can be found as:

$$\Delta k \geq 2 \times 10^7 (1/m) \quad (4.4)$$

CHAPTER 5

CONCLUSION AND FUTURE WORKS

The primary objective of this thesis is to exploit the near field diffraction technique that use structured light to estimate the sub-wavelength thickness of dielectric films on curved surfaces. For this purpose, various illumination sources and the near field measurement techniques were used in addition to the standard techniques.

The LBL assembly technique is used for the coating process because of the fact that the thickness of dielectric film has to be in sub-wavelength scale. The thickness of film can be increased in nanometer scale by choosing material via ph degree. Every coating cycle changes the thickness about 3 nanometers up to 40 nanometers. Thus, the process is optimized for fiber optic coating.

The total PSF of an optical system can be described as the multiplication of PSFs of the source and film. It means that if the PSF of source is modified, the total system PSF can be altered. To examine the effects of various light sources on the diffraction pattern, the structured lights generated by optical fiber modes were used. In this way, it is aimed to increase the phase contribution of dielectric film on the resultant diffraction pattern.

To observe the sharp and well defined transitions on the diffraction patterns, there is needed to use high order components. However, the high order components are lost at the far field observations since they are inversely proportional with distance. Studying at very close proximity to the film is a key parameter to detect the small variations. Therefore, the diffraction pattern were recorded at as close as possible to the sensor array in the proposed system.

In the near field measurements, pixel size determines the detection limits since quick and sharp variations occurs on the diffraction pattern. For this reason, the sensor selection has critical role in the measurements. In the measurement part of this thesis, the sensor array which has $1.12\mu m \times 1.12\mu m$ was used. Although measurements showed that transitions between discrete points on the diffraction patterns are bigger than $1.12\mu m$, the sensor array has capability to detect variations up to $1.12\mu m$.

The results have shown that the profile of illumination source has a key role for resolution since narrower PSF provides better resolution. The difference on diffraction patterns for the film of one-tenth of the wavelength thickness can not be observable for plane wave and LP01 mode sources. However, the thickness becomes detectable with

LP11 mode. The reason is that the PSF of LP11 is narrower when it compares with other sources. The intensity of LP11 mode has two lobes and they increase the phase contribution of dielectric film on the diffraction pattern. Besides, the sharp deviations can be seen by taking the high frequency components in the near field region. As a result, the divergence on the diffraction patterns becomes observable and measurable up to 67 nanometer according to the simulation and experimental results. Also simulation results show that it is not feasible to measure the coating thickness below 50 *nm*.

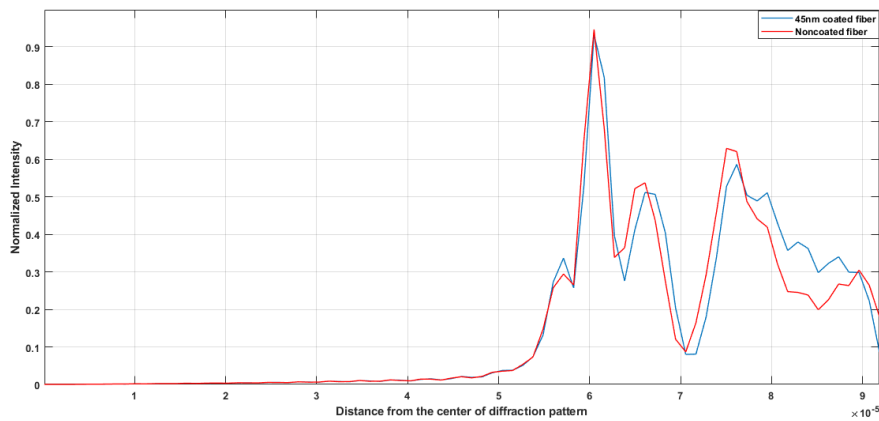


Figure 5.1. LP11 mode simulation results of non-coated and 45 nm coated optical fibers

For the future works, the characterization of thickness is important for especially Surface Plasmon Resonance Sensors (SPR) (Prawobo et al., 2018). Since sensitivity of sensor has correlation with the thickness of dielectric material, the thickness has to be measured precisely (Rani, 2014). Therefore, this technique can be useful for SPR sensors. Furthermore, different modes (ex:LP02) and quantum dots can be used as an excitation source or NA of system can be increased to obtain better resolution. In this way, the thickness below 50 *nm* might be observed.

In conclusion, the near field diffraction by using structured light may be practical and alternative method for the characterization of nano-scale dielectric films on curved surfaces.

REFERENCES

- Andrews, C. (1951). A correction to the treatment of fresnel diffraction. *American Journal of Physics* 19, 280.
- Balanis, A. C. (2012). *Advanced Engineering Electromagnetics* (2nd ed.). Wiley.
- Boncek, R. and D. Rode (1991). Far field radiation and modal dispersion of 1310 nm dispersion optimized fiber at 850 nm. *Journal of Lightwave Technology* 9, 18–21.
- Born, M. and E. Wolf (1999). *Principles of Optics* (7th ed.). Cambridge University Press.
- Buck, J. A. (2004). *Fundamentals of Optical Fibers* (2nd ed.). Wiley-Interscience.
- Carminati, R. Optics beyond the diffraction limit. An optional note.
- Ekici, C. (2016). *Optical characterization of dielectric films on curved surfaces using diffraction method*. Ph. D. thesis, Izmir Institute Of Technology.
- Ekici, C. and M. S. Dinleyici (2017). A practical approach for optical characterization of a film coated on the optical fiber. In *Optical Fiber Technology*, Volume 36, pp. 382–386. Elsevier.
- Enderlain, J. (2000). Theoretical study of detection of a dipole emitter through an objective with high numerical aperture. *Optics Letters* 25(9), 634–636.
- Gambling, W., D. Payne, H. Matsumura, and R. Dyott (1976). Determination of core diameter and refractive index difference of single-mode fibres by observation of the far field pattern. *IEE Journal on Microwaves, Optics and Acoustics* 1, 13–17.
- Gloge, D. (1971). Weakly guided fibers. *Applied Optics* 10(10), 2252–2258.
- Goodman, J. W. (1996). *Introduction to Fourier Optics* (2nd ed.). The McGraw-Hill Companies.

- Harrington, R. F. (2001). *Time-Harmonic Electromagnetic Fields* (2nd ed.). Wiley-IEEE Press.
- Huygens, C. (1690(1912)). *Treatise on light : in which are explained the causes of that which occurs in reflexion, and in refraction, and particularly in the strange refraction of iceland spar.*
- Kowarz, M. W. (1995). *Diffraction Effects in the Near Field*. Ph. D. thesis, The Institute of Optics.
- Mahan, J., N. Vinh, V. Ho, and M. N.B. (2018). Monte carlo ray trace diffraction based on the huygens fresnel principle. *Applied Optics* 57, 56–62.
- Makris, K. G. and D. Psaltis (2011). Huygens-fresnel diffraction and evanescent waves. *Optics Communications* 284, 1686–1689.
- Miller, D. A. B. (1991). Huygen’s wave propagation principle corrected. *Optics Letters* 16(18), 1370–1372.
- Novotny, L. and B. Hecht (2012). *Principles of Nano Optics* (2nd ed.). Cambridge University Press.
- Prawobo, B. A., A. Purwidyantri, and K.-C. Liu (2018). Surface plasmon resonance optical sensor: A review on light source technology. *Biosensors* 8, 80.
- Rani, M. (2014). *Studies On Surface Plasmon Resonance Based Fiber Optic Sensors*. Ph. D. thesis, Jaypee Institute Of Information Technology.
- Renoirt, J.-M., C. Zhang, M. Debliquy, M.-G. Olivier, P. Mégret, and C. Caucheteur (2013). High-refractive-index transparent coatings enhance the optical fiber cladding modes refractometric sensitivity. *Optics Express* 21(23), 29073–29082.
- Richardson, J. J., M. Bjornmalm, and F. Caruso (2015). Technology-driven layer by layer assembly of nanofilms. *Science* 348, aaa2491.
- Sabatyan, A. and M. T. Tavassoly (2007). Application of fresnel diffraction to nondestructive measurement of the refractive index of optical fibers. *Optical Engineer-*

ing 46, 128001–128001–7.

Sardela, M. (2014). *Practical Materials Characterization* (1th ed.). Springer-Verlag New York.

Saxena, M., G. Eluru, and S. S. Gorthi. Structured illumination microscopy. *Advances in Optics and Photonics* 7.

Severin, I., M. Poulain, and R. El Abdi (2007). Mechanical and chemical damage of optical fiber polymer coating. *Journal of Optoelectronics and Advancement Materials* 9(7), 2110–2115.

Tavassoly, M. T., A. Darudi, H. R. Khalesifard, and M. R. S. Hossaini (2001). Applications of fresnel diffraction from phase objects. In *The International Society for Optical Engineering*, Volume 4399. SPIE.

Vangindertael, J., R. Camacho, W. Sempels, P. Dedecker, and K. Janssen (2018). An introduction to optical super-resolution microscopy for the adventurous biologist. *Methods and Applications in Fluorescence* 6.

Volpe, F., P. Letourneau, and A. Zhao (2018). Huygens fresnel wavefront tracing. In *Computer Physics Communications*, Volume 212. Elsevier.

Wojcik, A. B., M. J. Matthewson, K. T. Castelino, J. Wojcik, and A. Walewski (2006). Hybrid glass coatings for optical fibers: effect of coating thickness on strength and dynamic fatigue characteristics of silica fibers. In *Reliability of Optical Fiber Components, Devices, Systems, and Networks III*, Volume 6193. SPIE.

Yang, Y. H., M. Haile, T. Y. Park, F. A. Malek, and J. C. Grunlan (2011). Super gas barrier of all-polymer multilayer thin films. *Macromolecules* 44, 1450–1459.

Yang, Y. H., F. A. Malek, and J. C. Grunlan (2010). Influence of deposition time on layer-by-layer growth of clay-based thin films. *Ind. Eng. Chem. Res* 49, 8501–8509.

Zang, L., H. Liu, E. Zhao, J. Qui, and J. Shen (2012). Drying and nondrying layer-by-layer assembly for the fabrication of sodium silicate/tio₂ nanoparticle composite films. *Langmuir* 28, 1816–1823.